From material to structure: Multi-scale damage and fracture interpretation using acoustic emission and integrated experimental techniques

Original
From material to structure: Multi-scale damage and fracture interpretation using acoustic emission and integrated experimental techniques / Jiang, Z.; Zhu, Z.; Lacidogna, G.; Chen, J.; Yang, Y.. - In: CONSTRUCTION AND BUILDING MATERIALS. - ISSN 0950-0618. - STAMPA. - 531:(2026), pp. 1-21. [10.1016/j.conbuildmat.2026.146704]

Publisher:
Elsevier

Published
DOI:10.1016/j.conbuildmat.2026.146704

Construction and Building Materials 531 (2026) 146704

Contents lists available at ScienceDirect

Construction and Building Materials

journal homepage: www.elsevier.com/locate/conbuildmat

From material to structure: Multi-scale damage and fracture interpretation using acoustic emission and integrated experimental techniques

Zihan Jiang [a,b], Zhiwen Zhu [a,*], Giuseppe Lacidogna [b,c,**], Jueliang Chen [c], Yang Yang [d]

[a] Department of Civil Engineering and Smart Cities, Shantou University, University Road 243, Shantou 515063, China
[b] Department of Structural, Geotechnical and Building Engineering, Politecnico di Torino, Corso Duca degli Abruzzi 24, Torino 10129, Italy
[c] College of Architecture and Energy Engineering, Wenzhou University of Technology, Wenzhou 325000, China
[d] School of Civil Engineering, Chongqing University, Chongqing 400045, China

ARTICLE INFO

Keywords:
Acoustic emission
Multi-scale damage
Fracture mechanics
Size effects
UHPC
Structural health monitoring
Critical phenomena

ABSTRACT

The interpretation of damage and fracture processes in cement-based materials and structures remains a fundamental challenge for ensuring the safety and durability of civil infrastructure. This paper presents a coherent synthesis of original experimental research unified by a methodological framework: the integration of Acoustic Emission (AE) monitoring with complementary techniques, including Digital Image Correlation (DIC), mechanical testing, and advanced signal analysis, to investigate fracture phenomena across multiple scales. This work presents a clear progression from material-scale behaviour to element-level response and full-scale structural applications. At the material scale, size effects and ductile-to-brittle transitions in plain concrete under compression are examined, revealing fractal energy emission characteristics. At the element scale, the damage process in GFRP-bar reinforced concrete beams is analysed through multi-technical approaches, including RA-AF analysis, natural time analysis, AE entropy, and the novel Method of Critical Fluctuations-Based (MCF-B). At the structural scale, two case studies demonstrate the practical application of AE monitoring: UHPC-strengthened RC beams after 24 years of sustained loading, and crack evolution monitoring on the UHPC deck layer of a long-span cable-stayed bridge during construction. Across all scales, AE parameters, including b-value, β_t coefficient, natural time variance, and entropy, consistently provide robust precursors to critical damage states. The synthesis demonstrates that fracture processes, from microcrack nucleation to macro-crack propagation and structural instability, follow scale-invariant patterns that can be captured through AE monitoring. This integrated, multi-scale perspective offers a physically grounded framework for structural health monitoring and damage assessment, demonstrating that consistent damage indicators can be interpreted across scales within a unified methodology.

1. Introduction

Civil engineering structures are subjected to progressive deterioration throughout their service life. This deterioration manifests as damage accumulation that spans an extraordinary range of scales: from the nucleation of microcracks at the micrometre scale within the material microstructure, to the propagation of meso-scale cracks at interfaces, and ultimately to macro-scale structural instability that may lead to catastrophic failure [1,2]. Understanding and predicting this multi-scale damage evolution is one of the most fundamental challenges in structural engineering.

Concrete, as the most widely used construction material worldwide, exemplifies this multi-scale complexity, with its heterogeneous nature comprising cement paste, aggregates, interfacial transition zones, and often fibre reinforcement [3–5]. This creates a rich landscape for crack initiation and propagation [6–8]. The situation is further complicated when modern materials such as Ultra-High Performance Concrete (UHPC) or Fibre-Reinforced Polymer (FRP) reinforcement are introduced, as these materials exhibit fundamentally different fracture behaviours compared to conventional concrete [9–11].

---

[*] Corresponding author.
[**] Corresponding author at: Department of Structural, Geotechnical and Building Engineering, Politecnico di Torino, Corso Duca degli Abruzzi 24, Torino 10129, Italy.

E-mail addresses: zihan.jiang@polito.it (Z. Jiang), zhuzw@stu.edu.cn (Z. Zhu), giuseppe.lacidogna@polito.it (G. Lacidogna), 20230011@wzut.edu.cn (J. Chen), yangyangcqu@cqu.edu.cn (Y. Yang).

https://doi.org/10.1016/j.conbuildmat.2026.146704
Received 5 April 2026; Received in revised form 27 April 2026; Accepted 12 May 2026

Among the various non-destructive techniques available for damage assessment, Acoustic Emission (AE) monitoring occupies a unique position [12,13]. Unlike methods that interrogate the structure with externally applied energy, such as ultrasonic testing, AE passively listens to the elastic waves emitted by the material itself as cracks propagate [14,15]. This fundamental characteristic makes AE a direct probe of the fracture process: every AE signal corresponds to an irreversible damage process occurring within the material [16,17]. The physical basis of AE lies in fracture mechanics. When a crack propagates, the sudden release of strain energy generates transient elastic waves that propagate through the material [18,19]. These waves, detected by piezoelectric sensors placed on the structure's surface, carry information about the source mechanism, crack orientation, and energy release. By analysing the characteristics of AE signals, specifically their amplitude, frequency, energy, and timing, it becomes possible to reconstruct the evolution of damage in real time [20,21]. AE-based parameter analysis and classification methods have been applied to innovative materials such as high-strength coral aggregate reinforced concrete, demonstrating the versatility of this monitoring approach [22]. Furthermore, the combined use of AE and Digital Image Correlation (DIC) has been successfully extended to various quasi-brittle materials, including rock-shotcrete composites and self-compacting concrete under different loading conditions [23–25].

A recurring challenge in structural health monitoring is the extrapolation of laboratory-scale observations to full-scale structures. Material-scale tests (on concrete cylinders or prisms) provide controlled conditions for understanding fundamental fracture mechanisms, but their direct applicability to real structures is often questioned due to size effects and boundary condition differences [26,27]. Conversely, field monitoring of in-service structures provides realistic data but lacks the controlled conditions necessary for mechanistic interpretation [28,29].

This paper argues that a coherent understanding of damage processes can only be achieved by bridging these scales through a unified experimental and analytical framework. The central thesis is that AE monitoring, when combined with complementary techniques such as DIC and interpreted through fracture mechanics principles, provides this unifying framework. The progression from material to element to structure is not merely a change in specimen size but a continuous evolution of fracture phenomena that follows scale-invariant laws.

This synthesis integrates a coherent series of experimental investigations that establish a clear trajectory from fundamental material behaviour to applied structural monitoring, forming a unified cross-scale framework for interpreting damage and fracture processes. The work progresses systematically across scales, demonstrating that damage evolution follows consistent and physically interpretable patterns from material to structural level, with AE serving as the unifying descriptor: at the material scale, the investigation of size effects on concrete compression failure combines AE and DIC to reveal fractal energy emission characteristics; at the element scale, a multi-technical analysis of damage processes in GFRP-bar reinforced concrete beams introduces advanced AE methods including RA-AF classification, natural time analysis, AE entropy, and the novel Method of Critical Fluctuations (MCF-B); and at the structural scale, two case studies demonstrate practical applications—the first presents a fracture mechanics analysis of RC beams strengthened with UHPC after 24 years of sustained loading, validating AE's capability to assess rehabilitation effectiveness, while the second involves field monitoring of crack evolution on the UHPC deck layer of a long-span cable-stayed bridge during construction, confirming the validity of AE techniques in real-world conditions.

Unlike previous studies that reported isolated experimental observations at single scales, this work provides the first systematic synthesis demonstrating that AE-based damage indicators follow scale-invariant patterns across six orders of magnitude in structural size, from 75 mm laboratory specimens to a 468 m cable-stayed bridge. The novelty lies not in individual datasets but in the unified cross-scale framework that reveals consistent critical transitions and fractal scaling laws governing damage evolution.

The paper is organized as follows: Section 2 presents the theoretical framework linking AE to fracture mechanics. Section 3 describes the integrated experimental methodologies employed across studies. Sections 4, 5, and 6 present results at the material, element, and structural scales, respectively. Section 7 provides a unified discussion synthesizing the cross-scale findings, highlighting the consistency of damage indicators and their interpretation within a single physically grounded framework.

2. Theoretical framework: acoustic emission and fracture mechanics

2.1. Fracture mechanics foundations

The fracture behaviour of quasi-brittle materials such as concrete is characterized by the formation and growth of a fracture process zone (FPZ) ahead of the crack tip [30]. Within this zone, energy is dissipated through microcracking, aggregate interlock, and fibre bridging. Unlike perfectly brittle materials where fracture is described by a single energy release rate, quasi-brittle fracture involves distributed damage that evolves with loading [31].

From an energetic perspective, the total energy released during fracture, R, can be decomposed as $R = D + E$ [32], where D represents the energy dissipated through inelastic processes (heat, plastic deformation) and E is the energy emitted as elastic waves, precisely the energy detected by AE sensors. This fundamental relationship establishes AE as a direct measure of the dynamic energy release during crack propagation, providing a physically grounded link between experimental observations and fracture mechanics across scales.

2.2. AE parameters and fracture mode classification

AE waveforms contain multiple parameters that can be related to source characteristics [33,34]. As shown in Fig. 1, the amplitude (A), defined as the maximum voltage of the AE signal, is directly related to the magnitude of the source signal, with larger crack jumps producing higher amplitude signals. Rise time (RT) measures the interval from the first threshold crossing to the peak amplitude and is influenced by both the source mechanism and the wave propagation path. Duration (DT) represents the time elapsed between the first and last threshold crossings, reflecting the duration of the source signal. Ringing count (RC) quantifies the number of times the signal exceeds the threshold, providing a measure of signal complexity. From these primary parameters, two derived indicators are commonly employed: average frequency (AF), calculated as the ratio RC/DT and expressed in kHz, reflects the frequency content of the signal (see Eq.1), while rise angle (RA), defined as the ratio RT/amplitude and expressed in ms/V, is particularly sensitive to the fracture mode (see Eq.2). When analysed collectively, these parameters provide a characteristic fingerprint of the underlying fracture mechanism.

The morphology of AE waveforms contains information about the fracture mode [35,36]. Tensile cracks (Mode I) generate signals with high average frequency and low rise angle, corresponding to sharp, impulsive waveforms. Shear cracks (Mode II) produce signals with lower frequency and higher rise angle, reflecting the more gradual nature of shear displacement.

The RA-AF method classifies signals based on these parameters, enabling real-time tracking of the dominant fracture mechanism throughout loading. This capability is particularly valuable for understanding transitions in failure modes, such as the shift from distributed microcracking to localized shear failure.

$$AF = \frac{RC}{DT} \quad \frac{(Ringing\ Count)}{(Duration\ Time)}, \tag{1}$$

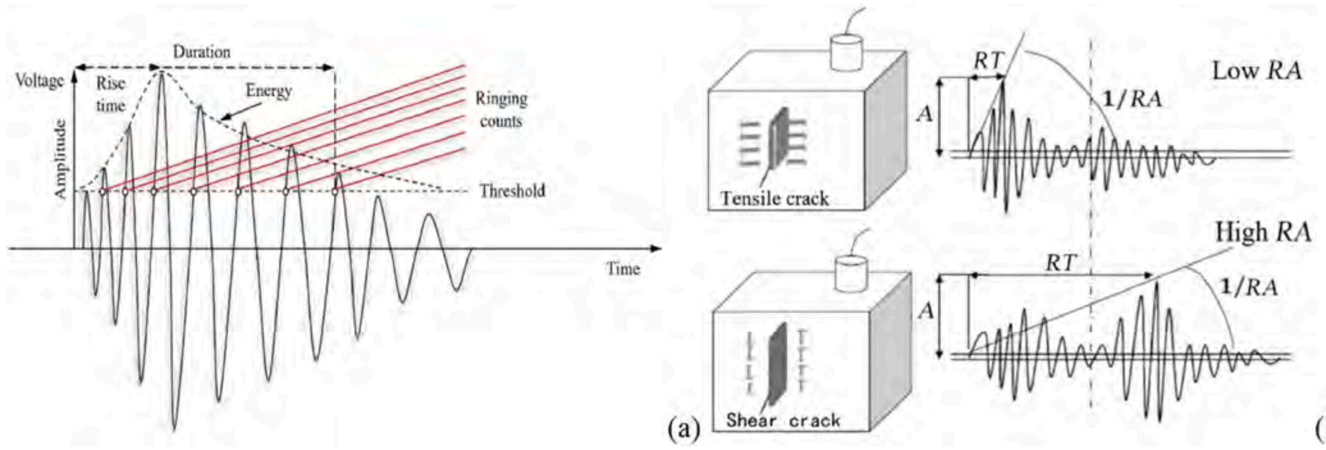

Fig. 1. Tensile (Mode I) and shear (Mode II) cracks. (a) AE waveform parameters; (b) Crack type.

$$RA = \frac{RT(RiseTime)}{A_{\max}(Amplitude)}. \tag{2}$$

In this study, the threshold between tensile and shear cracks was not defined by a fixed empirical value. Rather, a K-means clustering algorithm was applied to the RA and AF parameters of the AE signal population for each dataset individually, yielding a data-driven separation line that reflects the intrinsic distribution of the signals.

2.3. The Gutenberg-Richter law and b-value analysis

A fundamental observation in both seismology and AE analysis is that the frequency-magnitude distribution of events follows a power law [37,38]:

$$\log \quad N(\geq A) = a - b\log A \tag{3}$$

where N is the number of signals with amplitude greater than A, and a and b are empirical constants. The b-value, representing the slope of this distribution, reflects the relative proportion of small to large events.

Within the framework of fracture mechanics, the b-value carries a distinct physical interpretation, where its variation directly reflects the evolving damage state [39,40]. High b-values, typically greater than 1.5, signify a predominance of microcracks and are characteristic of diffuse damage. As damage accumulates, a decrease in the b-value towards 1.0 signals the coalescence of these microcracks into larger macrocracks, marking the onset of critical crack propagation. A further decline to values below 1.0 is ultimately associated with unstable fracture and serves as a precursor to impending failure.

2.4. Critical phenomena and natural time analysis

The approach to failure in complex systems is often preceded by characteristic fluctuations that signal criticality. Natural time analysis, originally developed for seismic electrical signals [41,42], provides a framework for detecting such critical states in AE time series.

In natural time χ, the order of signals becomes the relevant temporal coordinate. The variance of natural time, κ_1, is defined as [43]:

$$\kappa_1 = \sum\nolimits_{k=1}^{N} p_k {\chi_k}^2 - \left(\sum\nolimits_{k=1}^{N} p_k \chi_k\right)^2 = \langle \chi^2 \rangle - \langle \chi \rangle^2 \tag{4}$$

where $\chi_\mathrm{k} = k/N$ is the normalized order of the k-th signal, and p_k is the normalized energy of that signal. When a system approaches criticality, κ_1 converges to 0.07, providing a robust precursor to failure independent of the specific loading conditions [44].

In particular, two conditions have been defined for identifying the transition of the monitored structure to a critical state: (I) The parameter κ_1 is approaching the value 0.07 "by descending from above"; (II) The entropies S and S_rev are lower than the entropy of the uniform noise, which is S_u= 0.0966. The entropy S is defined as:

$$s = \langle \chi \ln \chi \rangle - \langle \chi \rangle \ln \langle \chi \rangle, \mathrm{where} \langle \chi \ln \chi \rangle = \sum\nolimits_{k=1}^{N} \chi_k p_k \ln \chi_k \tag{5}$$

Similarly, the entropy S_rev is obtained by considering the time reversal $T_{PK} = P_{N\_K+1}$.

Therefore, when the conditions (I) and (II) are satisfied, the time is found, at which the criticality occurs in the monitored structure [45].

While the critical value $\kappa_1 = 0.07$ is theoretically predicted as a universal constant for systems approaching criticality, the observability and temporal width of the critical window may be influenced by material composition. For fibre-reinforced members, the bridging effect of fibres tends to prolong the critical transition, resulting in a broader plateau where κ_1 remains near 0.07. Nonetheless, the threshold value itself remains scale- and material-invariant.

2.5. The method of critical fluctuations-based (MCF-B)

The classical b-value analysis assumes a pure power-law distribution of signal amplitudes. However, many experimental observations reveal deviations from this ideal behaviour, particularly as failure approaches [46]. The Method of Critical Fluctuations based approach (MCF-B) addresses this limitation by introducing a dual-exponent model [47]:

$$N(A) = \quad p_1 \cdot A^{-p_2} \quad \cdot e^{-Ap_3} \tag{6}$$

Here, p_2 represents the power-law decay exponent (analogous to the b-value), while p_3 captures exponential deviations. The transition to criticality is characterized by a decrease in p_2 accompanied by a monotonic increase in p_3, signalling the crossover from power-law to exponential-dominated behaviour that precedes failure.

The proposed MCF-B method is implemented through an iterative procedure applied to the AE time series. First, for an initial data set comprising signals #1 to #B, a histogram of AE amplitudes is calculated. This distribution, N(A), is then plotted on a log-log scale and fitted using the function presented in Eq.(6) to determine the corresponding exponents p_2 and p_3. Subsequently, as each new signal occurs, the dataset is expanded incrementally to include signals #1 through #B+ 1, and the fitting process is repeated. This stepwise progression allows for the continuous rescaling and tracking of the exponents p_2 and p_3 throughout the entire duration of the AE data up to the point of failure.

In the MCF-B approach, criticality is identified by the evolution of the fitting exponents p_2 and p_3 in the amplitude distribution. A system approaching failure typically exhibits [47]: (I) The presence of a “perfect” power law (that is $p_2 > 1$ and $p_3 \approx 0$); (II) Followed by the decrease of p_2 and the monotonic increase of p_3. In fact, the behaviour of the exponents of the MCF-B approach reveals a crossover phenomenon when the system is close to failure.

2.6. *Fractal scaling of energy emission*

The damage process in heterogeneous materials exhibits fractal characteristics [48,49]. The energy emitted during fracture, E, scales with specimen size according to:

$$E \propto V^{D/3} \tag{7}$$

where V is the specimen volume and D is the fractal dimension. When $D = 3$, damage is uniformly distributed throughout the volume; when $D = 2$, damage localizes on a preferential surface. This indicates that the fractal energy density Γ (having non-integer physical dimensions) can be considered as the size-independent parameter:

$$\Gamma = \frac{E}{V^{D/3}} \tag{8}$$

Furthermore, AE can be detected during microcrack propagation. The energy emission, E, is proportional to the total number N of AE signals. Accordingly, the total number of AE signals, $N_{\max}$, over a fractal domain, can be considered as the size-independent parameter:

$$\Gamma_{AE} = \frac{N}{V^{D/3}} \tag{9}$$

where Γ_{AE} is the value of AE signals fractal density. This scaling law provides a quantitative link between laboratory observations and structural-scale behaviour.

3. Integrated experimental methodology

3.1. *Common monitoring framework*

Across all studies presented in this synthesis, a consistent experimental philosophy was applied: the integration of AE monitoring with complementary techniques to provide multi-faceted insight into damage processes. Table 1 summarizes the experimental configurations across scales.

3.2. *Acoustic emission instrumentation*

For AE monitoring across all experimental campaigns, piezoelectric sensors with a frequency response range of 10 kHz to 1 MHz were employed. Data acquisition was performed using the ÆMISSION® system developed by Lunitek (Italy), which features a 10 MHz sampling rate per channel, 60 dB pre-amplification, and programmable threshold triggering [50]. Additionally, the system's wireless data transmission capability facilitated its deployment in both laboratory settings and the field monitoring application discussed in Section 6.2.

Although the sensors possess a nominal frequency response from 10 kHz to 1 MHz, all recorded signals were band-pass filtered between 20 kHz and 400 kHz prior to analysis. This filtering strategy retains the dominant frequency range of crack-related AE signals in cementitious materials while effectively suppressing low-frequency ambient noise from wind, traffic, and mechanical operations, as well as high-frequency electronic interference.

Sensors were coupled to specimen surfaces using silicone resin or vacuum grease to ensure acoustic transmission. Threshold levels were established based on pre-test background noise characterization, typically set at 2 mV to filter ambient noise while retaining crack-related signals.

3.3. *Digital image correlation*

DIC was employed as a complementary technique to AE, providing full-field surface displacement and strain measurements [51,52]. Specimen surfaces were prepared with random speckle patterns (5–7 pixel speckle size) using matte black and white paint. During loading, tripod-mounted cameras positioned perpendicular to the surface captured images at frequencies synchronized with test progression, with acquisition rates adjusted according to loading speeds to record crack initiation and propagation. As illustrated in Fig. 2, the DIC principle involves dividing the reference image into sub-regions, which are then independently tracked and compared with subsequent images to analyse the overall deformation field. The irregular speckle patterns enable accurate subset tracking throughout the loading process. Post-processing using correlation algorithms yielded displacement fields and strain maps that provided direct visual evidence of crack development and strain localization.

The spatial resolution ranged from approximately 0.04 mm/pixel for the 75 mm specimens to 0.16 mm/pixel for the 300 mm specimens. At this resolution, while individual microcracks with opening displacements below 0.01 mm may not be directly resolved, the strain localization bands associated with microcrack clustering are reliably detectable. This complementary sensitivity between DIC and AE, where AE detects microcrack nucleation at earlier stages and DIC captures subsequent strain localization, enables cross-validation of the damage evolution sequence.

3.4. *Mechanical loading protocols*

Mechanical loading protocols were tailored to the specific scale and

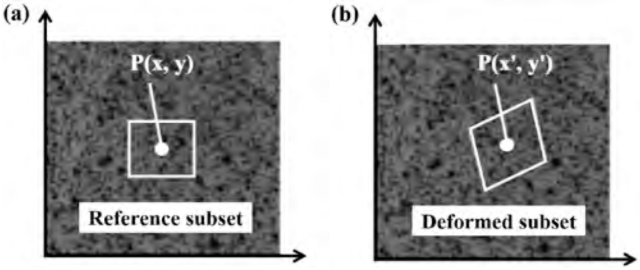

Fig. 2. Schematic of speckle displacement principle for DIC: (a) Reference subset, and (b) Deformed subset.

Table 1
Summary of experimental configurations across scales.

Scale	Specimens	Dimensions	AE Sensors	Complementary Techniques	Key Parameters
Material	Plain concrete cubes	75, 150, 300 (mm)	1	DIC, load-displacement	*b*-value, fractal dimension, cumulative AE
Element	GFRP-RC beams	1800 × 200 × 200 (mm)	2	DIC, strain gauges, CMOD	RA-AF, natural time, MCF-B, AE entropy
Structure I	UHPC-strengthened RC beams	2000 × 150 × 100 (mm)	4	Strain gauges, LVDTs	*b*-value, β_t, natural time, RA-AF
Structure II	UHPC bridge deck (field)	468 m main span (local cracked region only)	4	Crack measurements, traffic data	*b*-value, β_t, source location

objectives of each experimental investigation. At the material scale, displacement-controlled compression tests were conducted at a rate of 0.01 mm/s, with Teflon layers applied at the loading interfaces to minimize frictional end effects. For the element-scale study on GFRP-reinforced beams, a four-point bending configuration was employed under Crack Mouth Opening Displacement (CMOD) control, with an initial loading rate of 0.05 mm/min that was increased to 0.2 mm/min once a crack opening of 0.1 mm was achieved. At the structural scale, laboratory tests on UHPC-strengthened beams were performed under monotonic four-point bending up to failure. Complementing these controlled experiments, the field study involved passive AE monitoring of a cable-stayed bridge deck during its construction phase, capturing damage evolution under ambient conditions and construction vehicle loading.

3.5. Data analysis protocols

Across all studies, AE data analysis followed a consistent multi-step protocol. The initial pre-processing stage involved threshold-based filtering, removal of electrical noise characterized by signals with duration below 3 μs and counts fewer than 3, and band-pass filtering between 20 and 400 kHz to retain crack-related signals while suppressing ambient disturbances. Following pre-processing, key AE parameters were extracted, including amplitude, rise time, duration, counts, energy, as well as the derived RA (rise angle) and AF (average frequency) values. Statistical analysis was then performed, comprising *b*-value calculations using moving windows of 50–100 signals and determination of the β_t coefficient through power-law fitting of cumulative AE signals. For criticality assessment, natural time analysis was conducted with window sizes ranging from 50 s to 100 signals, complemented by MCF-B analysis employing cumulative window progression to track the evolution of scaling exponents. Finally, source localization via triangulation based on arrival time differences was performed exclusively for the field study, where sensor geometry permitted spatial identification of active crack sources.

The selected AE preprocessing parameters and window settings were not arbitrarily defined but based on pre-test background noise characterization, established practices for cement-based materials, and a trade-off between statistical significance and temporal resolution. A cross-scale internal consistency check was performed across material, element and structural datasets, confirming that the reported trends, including *b*-value decrease towards 1.0, natural time variance approaching 0.07, and critical transition identification, remain stable under moderate variations of threshold (±0.5 mV), filter cut-offs (10–30 kHz / 350–450 kHz), and window sizes (30–150 events).

In this manuscript, the term 'AE signal' (or 'AE hit') refers to a threshold-crossing waveform recorded by a sensor. The term 'AE event' is reserved for cases where source localization has been performed to associate multiple signals with a common physical source; this occurs only in the field study presented in Section 6.2. In laboratory experiments without source localization, we consistently use 'AE signal' to avoid ambiguity.

4. Material scale: size effects in concrete compression failure

4.1. Experimental design and motivation

Understanding size effects is fundamental to extrapolating laboratory observations to structural behaviour. At the material scale, as shown in Fig. 3, plain concrete specimens of three base sizes (75, 150, and 300 mm) and three slenderness ratios (λ = 0.5, 1.0, 2.0) were tested under uniaxial compression. Fig. 4 shows the experimental setup. The systematic variation in geometry allowed investigation of both size and shape effects on failure modes, strength, and energy release characteristics. While single specimens are presented for each size-slenderness combination, it is well established that strength depends on scale: smaller specimens of a quasi-brittle material contain fewer defects, leading to higher apparent strength [1]. Previous extensive analyses of concrete specimens with varying shapes and sizes have reported fractal dimensions for energy emission ranging between 2 and 3 (D ≈ 2.3) [1].

For the smallest specimens with a base size of 75 mm, a slenderness ratio λ = 0.5, and a height of 35 mm, the specimen height was comparable to the AE sensor dimension of approximately 35 mm in diameter. To prevent any mechanical interference between the loading platens and the sensors during compression testing, steel spacers (shims) were introduced between the specimen ends and the loading platens. This

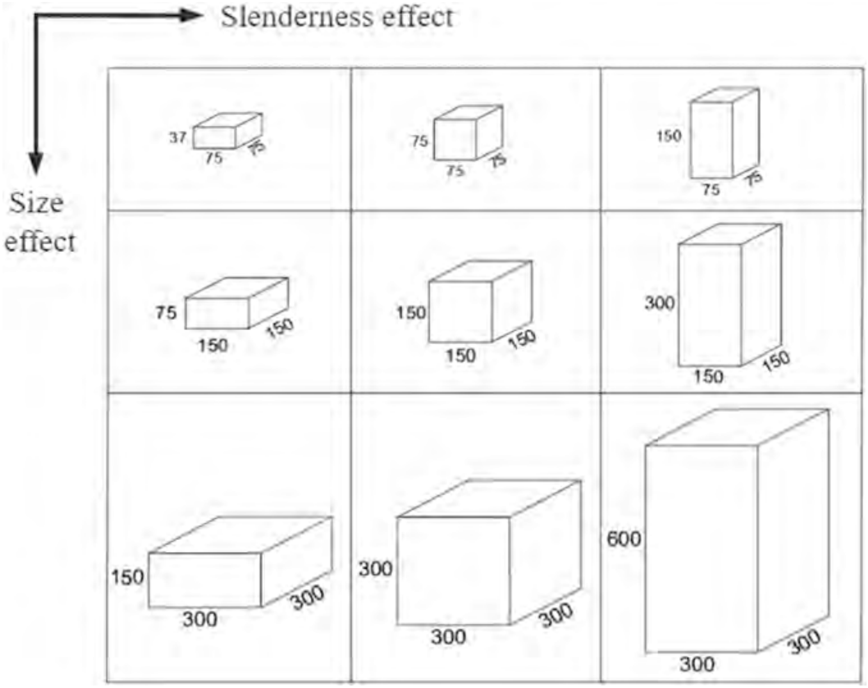

Fig. 3. Size-slenderness variation.

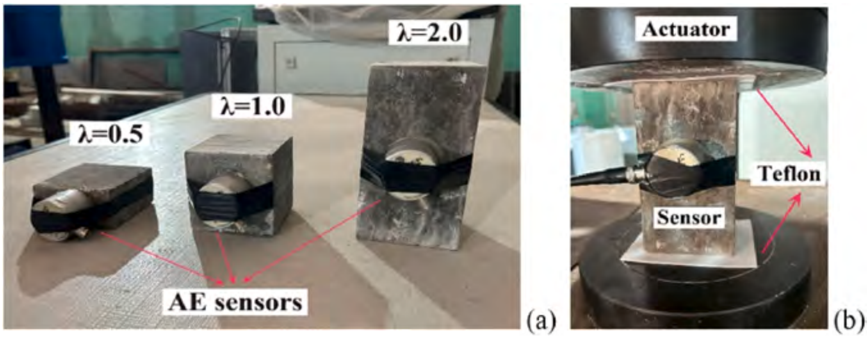

Fig. 4. AE sensor layout (a) and compression tests (b).

configuration provided sufficient clearance for the AE sensors and ensured that the recorded mechanical response was not affected by sensor-platen contact.

4.2. Size-slenderness effects on failure mode

Fig. 5 presents representative load-displacement curves and cumulative AE for specimens of different slenderness (λ = 0.5, 1.0, 2.0) with constant base size (150 mm). A clear transition in behaviour is observed with increasing slenderness: Stubby specimens (λ = 0.5) exhibited ductile post-peak softening, with gradual load decay. Cumulative AE increased progressively, reflecting continuous microcracking throughout the specimen; Intermediate specimens (λ = 1.0) showed a snap-back instability immediately after peak load, characterized by a sudden load drop and corresponding AE burst. This marks the transition from stable to unstable crack propagation; Slender specimens (λ = 2.0) displayed multiple snap-back instabilities in the post-peak regime, each coinciding with an AE burst. The final failure was governed by a dominant sub-vertical crack.

Table 2 quantifies the slenderness effect: as λ increased from 0.5 to 2.0, compressive strength decreased by 16.7%, while cumulative AE signals increased by 81.4%. This inverse relationship reflects the transition from crushing-dominated failure (high strength, low AE) to cracking-dominated failure (lower strength, high AE release).

4.3. Size effects on brittle-ductile transition

Fig. 6 shows results for specimens with constant slenderness (λ = 1.0) and varying base size (75, 150, 300 mm). With increasing size, the post-peak response transitioned from softening (75 mm) to snap-back instability (150 mm) to catastrophic snap-back (300 mm). This progression confirms that larger specimens exhibit more brittle behaviour, consistent with fracture mechanics predictions.

The size effect on strength, while present (2.7% reduction from 75 mm to 300 mm), was less pronounced than the effect on failure mode. However, the cumulative AE signals showed a dramatic increase with size: the 300 mm specimen emitted 6742 signals, approximately 25 times more than the 75 mm specimen (264 signals), despite its volume being 64 times larger. This disproportionate scaling provides crucial insight into the fractal nature of energy emission.

Table 2
Compressive strength and AE signals for different slenderness ratios (size = 150 mm).

Slenderness ratio (λ)	Compressive strength (MPa)	Strength reduction (%)	AE signals ($N_{\max}$)	Failure mode
0.5	36.4	-	982	Crushing-dominated
1	33.3	8.5	1406	Mixed crushing/ cracking
2	30.3	16.7	1781	Cracking-dominated

4.4. DIC observations of crack patterns

DIC strain fields (Fig. 7) revealed the underlying fracture mechanisms. The slender specimen (λ = 2.0) exhibited a dominant near-vertical crack with limited branching, characteristic of brittle fracture. In contrast, the stubby specimen (λ = 0.5) showed multiple distributed cracks with extensive branching, consistent with ductile crushing failure. These observations directly correlate with the AE characteristics: concentrated AE bursts in slender specimens versus distributed AE activity in stubby specimens.

4.5. Fractal analysis of emitted energy

The scaling of cumulative AE signals with specimen volume provides a quantitative measure of damage localization. Fig. 8 presents the log-

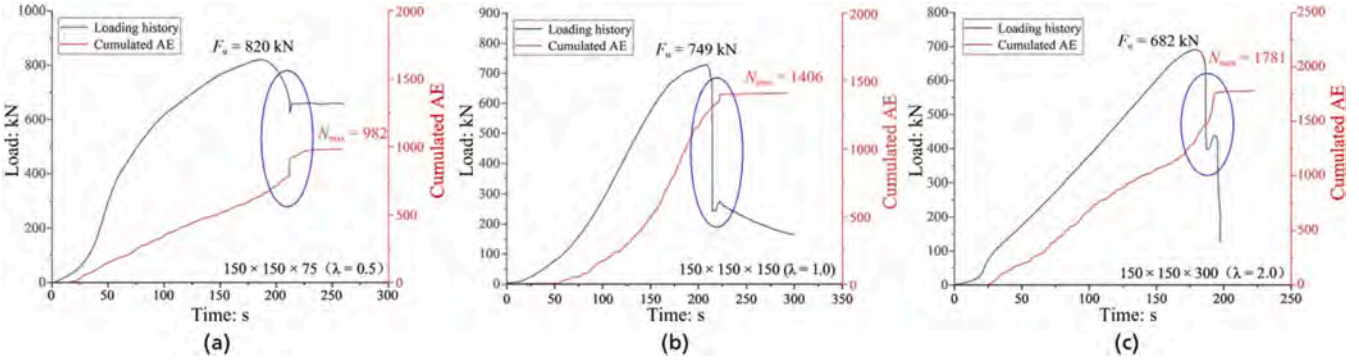

Fig. 5. Loading history and cumulated AE curves for concrete specimens of base size 150 mm and different slenderness ratios: (a) λ = 0.5; (b) λ = 1.0; (c) λ = 2.0.

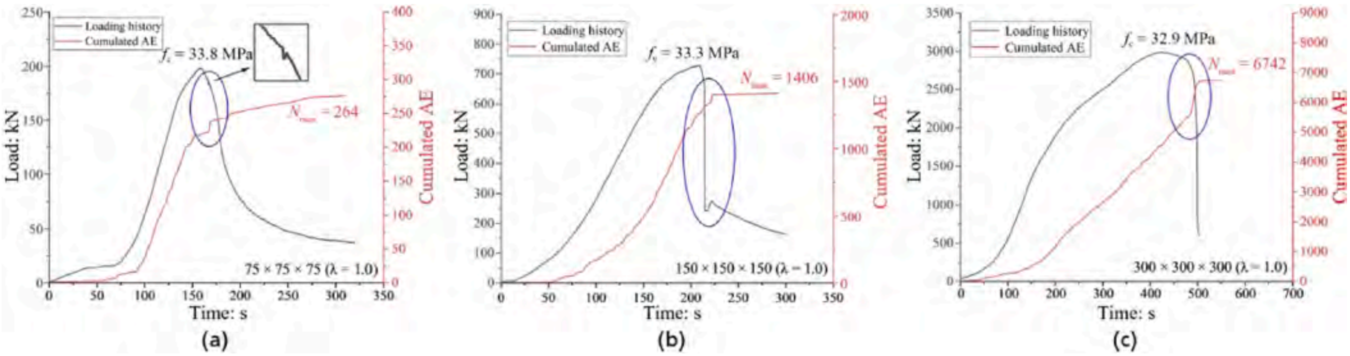

Fig. 6. Loading history and cumulated AE curves for concrete specimens with λ = 1.0 and different base sizes: (a) 75 mm; (b) 150 mm; (c) 300 mm.

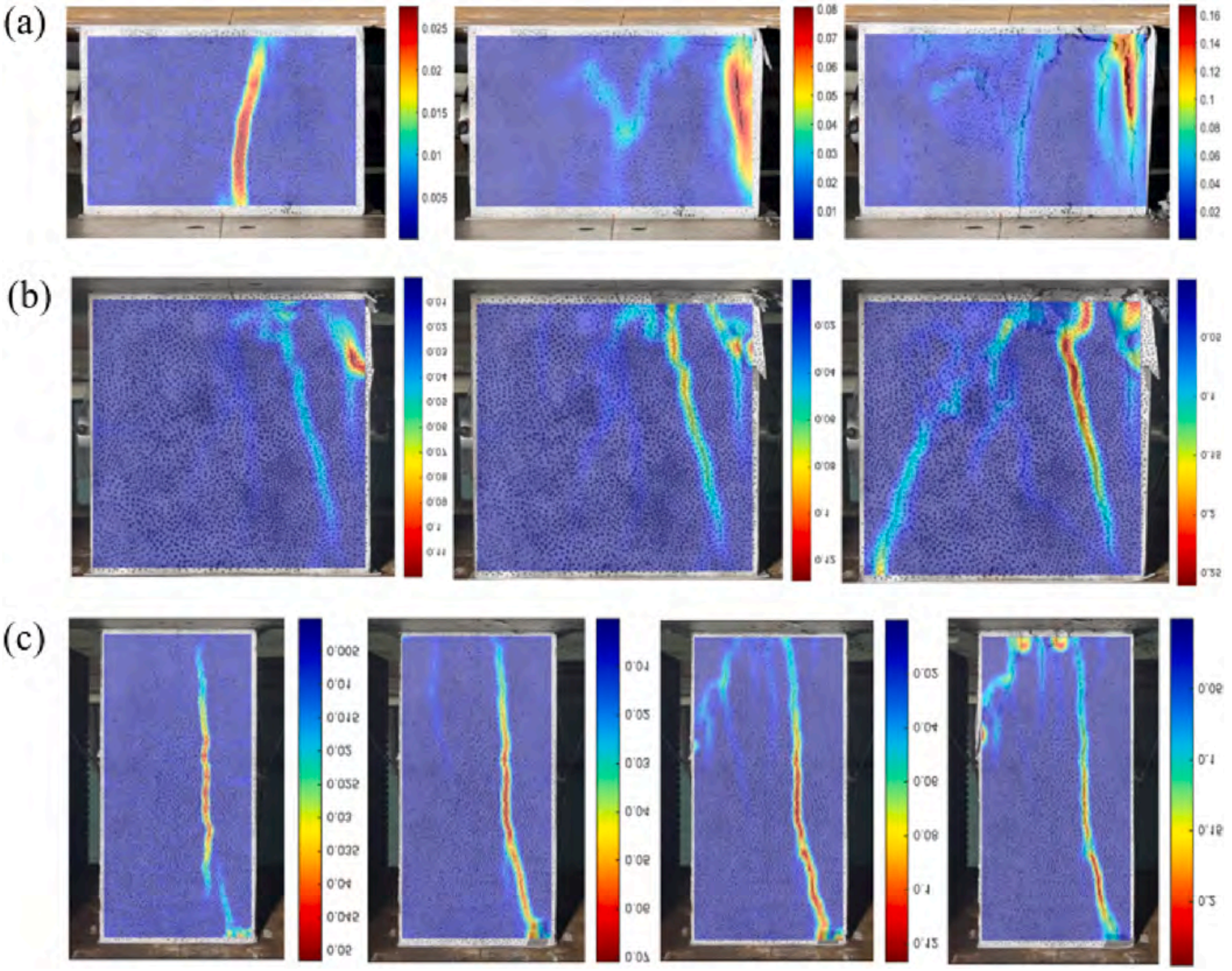

Fig. 7. DIC strain cloud diagram of the fracture process in concrete specimens of size 300 mm and different slenderness ratios: (a) λ = 0.5; (b) λ = 1.0; (c) λ = 2.0.

log relationship between N_{max} and specimen volume. The slope of 0.73 corresponds to a fractal dimension D = 2.19, indicating that energy emission occurs in a domain closer to a surface (D = 2) than to a volume (D = 3). This result is consistent with previous findings on the fractal nature of damage in concrete, where the morphological fractal dimension has been shown to correlate with the power-law exponent of energy emission [53,54].

This finding has profound implications for structural monitoring: damage in compression concentrates on preferential surfaces, and AE signals provide a direct measure of this localization. The fractal AE density of 4 signals per unit surface ($cm^{-2.19}$) offers a scale-independent parameter for damage characterization.

4.6. Implications for higher scales

The material-scale investigation establishes several fundamental

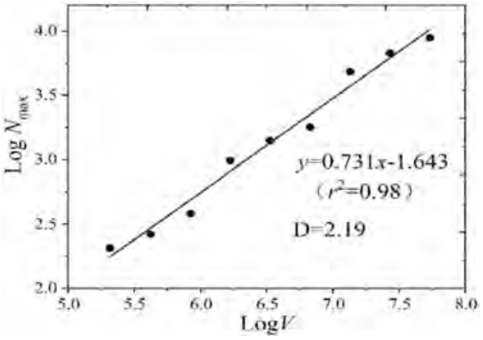

Fig. 8. Fractal domain of energy emission. The slope of 0.73 corresponds to fractal dimension D = 2.19.

principles that extend directly to larger scales, supporting the existence of scale-invariant damage mechanisms. First, damage localization emerges as a pervasive characteristic: fracture processes concentrate on preferential surfaces rather than distributing uniformly throughout the volume, a scaling property that persists across all structural dimensions. Second, the consistent correlation between each snap-back instability and a corresponding AE burst validates AE as a direct quantitative measure of dynamic energy release during fracture signals. Third, the observed size effects, wherein larger specimens exhibit increasingly brittle behaviour, emphasize the necessity for scale-aware monitoring strategies that account for structural dimensions when interpreting damage indicators. Finally, the crushing-to-cracking transition with increasing slenderness demonstrates how geometric parameters fundamentally influence failure mechanisms, a recurring theme that resurfaces at element and structural scales, confirming the continuity of damage processes within a unified interpretative framework.

5. Element scale: damage process in GFRP-bar reinforced concrete beams

5.1. Experimental context

Moving from plain concrete to reinforced elements introduces new complexities: the interaction between concrete and reinforcement, bond-slip mechanisms, and the potential for multiple crack types. The investigation of GFRP-bar reinforced concrete beams represents a logical progression from the material-scale studies, applying multi-technical analysis to a structural element with modern reinforcement materials.

GFRP bars offer advantages in corrosion resistance but exhibit fundamentally different mechanical behaviour compared to steel reinforcement: lower elastic modulus, linear elastic response to failure, and distinct bond characteristics [55]. These differences influence the damage evolution and failure mechanisms, providing an ideal test case for AE-based damage characterization.

The four-point bending test setup is illustrated in Fig. 9. The beam specimen had a total length of 1800 mm and a cross-section of 200 × 200 mm. A single GFRP bar (nominal diameter: 12 mm, rib spacing: 10 mm) was placed as the bottom flexural reinforcement, with an elastic modulus of 56.4 GPa and an ultimate tensile strength of 1164 MPa. To promote bond-slip failure at the GFRP-concrete interface, asymmetric unbonded lengths were designed: 150 mm on the left side and 50 mm on the right side, with a notch introduced at the midspan to induce localised damage. AE monitoring was performed using two piezoelectric sensors positioned along the GFRP bar direction (Fig. 9). Loading was displacement-controlled using an MTS system via CMOD control.

5.2. Global behaviour and stick-slip phenomena

Fig. 10 presents the load-time response of three nominally identical beams. The average peak load of 101.4 kN with low coefficient of variation (2.30%) confirms test reproducibility. Notably, saw-tooth-shaped load drops were observed prior to peak load, a signature of stick-slip behaviour at the GFRP-concrete interface.

The stick-slip mechanism arises from the intermittent loss and

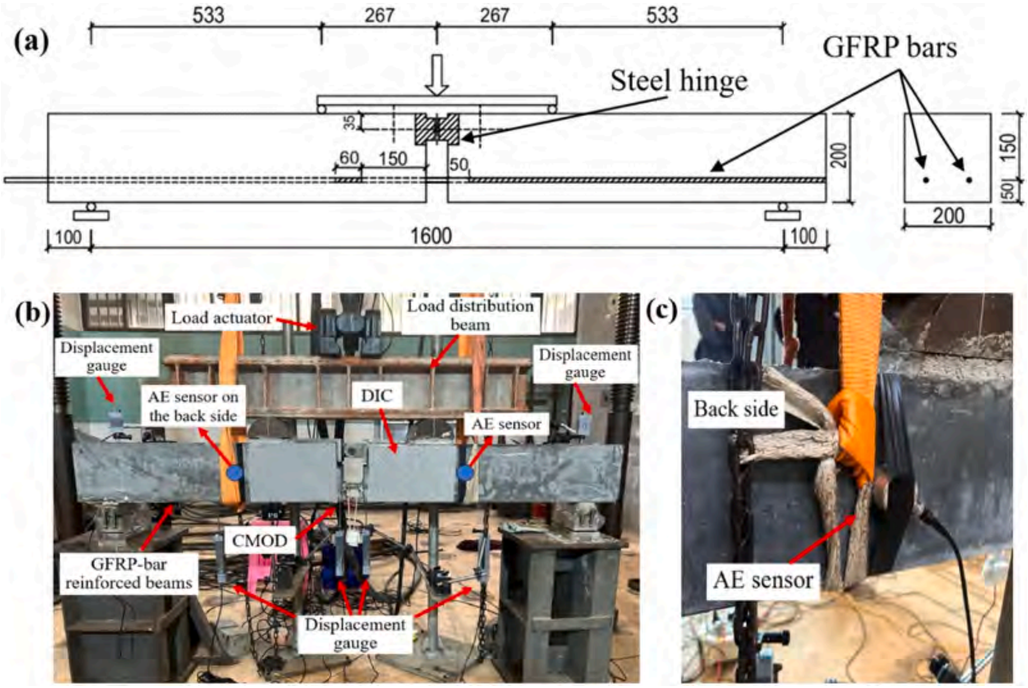

Fig. 9. Schematic of the GFRP-reinforced concrete beam (a,b) and AE sensor arrangement (c).

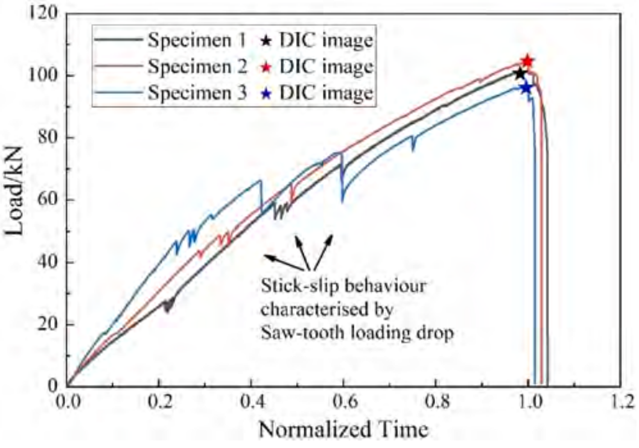

Fig. 10. Global behaviours of the test beams.

recovery of bond: local debonding causes sudden load drops, followed by re-engagement as load redistributes. Each slip signal releases elastic energy, generating high-amplitude AE signals. Fig. 11 demonstrates the correlation between AE amplitude peaks and load drops, with each major load drop corresponding to an AE burst.

5.3. *RA-AF analysis: tracking fracture mode evolution*

The RA-AF method provides insight into the changing fracture mechanisms throughout loading. Fig. 12 divides the damage process into stages based on stick-slip signals, while Fig. 13 presents the quantitative distribution of tensile (Mode I) and shear (Mode II) cracks. The dividing line in each sub-figure was determined by K-means clustering applied independently to the corresponding dataset; therefore, the slope and intercept vary across sub-figures according to the intrinsic signal distribution.

The evolution follows a consistent pattern across three distinct stages. During Stage TS1 (initial loading), approximately 80% of microcracks exhibit tensile characteristics, and distributed microcracking dominates the damage process. A significant shift occurs in Stage TS2 (first stick-slip), where the proportion of shear cracks increases markedly, transitioning the failure mode from tension-dominated to shear-dominated. By Stage TS3 (final loading), shear cracks predominate at a ratio of approximately 4:1 relative to tensile cracks, with transverse shear cracks developing preferentially near the GFRP bar at the notch. This progression from tensile to shear dominance is a hallmark of bond-slip failure in reinforced elements, where interfacial shear ultimately governs the final failure.

5.4. *Complementary DIC observations of crack localisation*

To further validate the fracture mode evolution identified by the RA-AF analysis and to visualise the spatial characteristics of the damage, DIC was employed. Fig. 14 presents the equivalent strain field and horizontal strain field for the three tested GFRP-bar reinforced concrete beams at the point of final failure.

The DIC results consistently reveal that crack development is predominantly concentrated in the vicinity of the GFRP bar within the notch region. Specifically, the horizontal strain field clearly delineates the morphology of transverse shear cracks, which align with the shear-dominated cracking behaviour identified in the later stages (Stage TS3) of the RA-AF analysis. No significant tensile cracks are observed in the DIC strain localisation patterns at this stage, corroborating the AE-based finding that the final failure is governed by shear rather than tension.

Moreover, the strain concentration zones observed via DIC correspond spatially to the location of intense AE activity reported in Fig. 11. This spatial correlation establishes a direct relationship between the AE signal characteristics and the underlying physical damage: areas exhibiting high shear strain localisation in DIC are the same areas generating high-amplitude, shear-type AE signals. Thus, the DIC measurements not only confirm the RA-AF classification results but also provide a direct visual link between the AE-based precursors and the actual crack geometry.

5.5. *Natural time analysis: detecting critical states*

Natural time analysis of AE energy series reveals the approach to criticality. Fig. 15a presents the evolution of variance κ_1 and entropies S and S_{rev} throughout loading. The critical region (grey background) is identified when two conditions are satisfied: κ_1 approaches 0.07 "by descending from above"; Entropies S and S_{rev} are lower than the uniform noise entropy $S_{\mathrm{u}} = 0.0966$. For the GFRP beam, this critical region occurs near normalized time 0.65, significantly before peak load. The structure has entered a terminal phase where damage processes become strongly correlated, though failure is not immediate; under displacement control, finite post-critical life remains.

5.6. *AE entropy: disorder as a damage indicator*

AE entropy quantifies the disorder in signal waveforms [56,57]. Fig. 15b shows entropy evolution with a window size of 50 signals. Low entropy indicates a more ordered system state—paradoxically, this order signals preparation for failure as damage localizes.

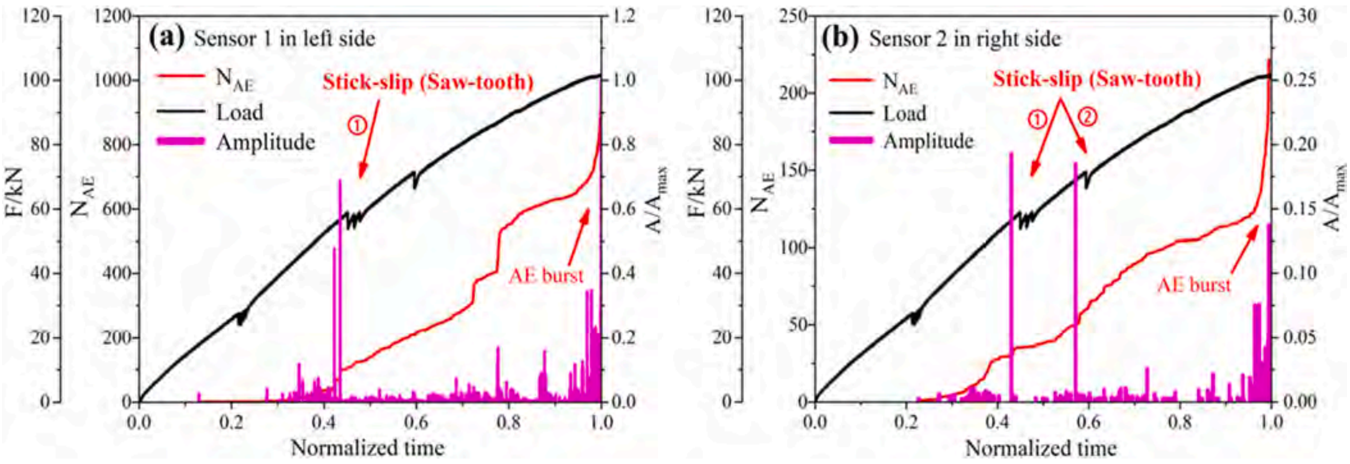

Fig. 11. Comparison of AE signals on left (a) and right (b) sides of the test beam.

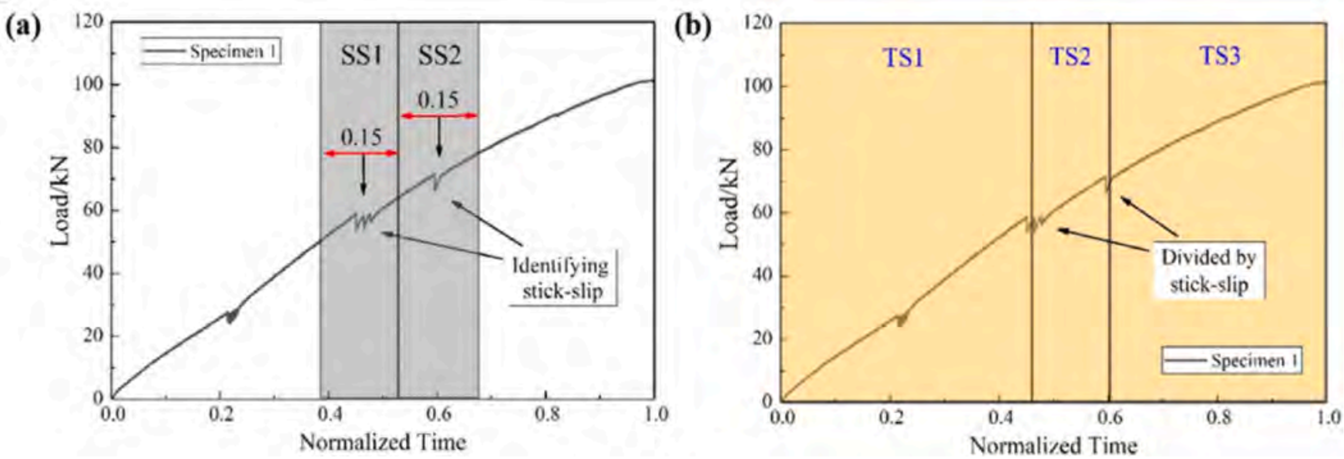

Fig. 12. Damage stage divisions for RA-AF analysis: (a) two divisions for identifying stick-slip; (b) three divisions for damage process.

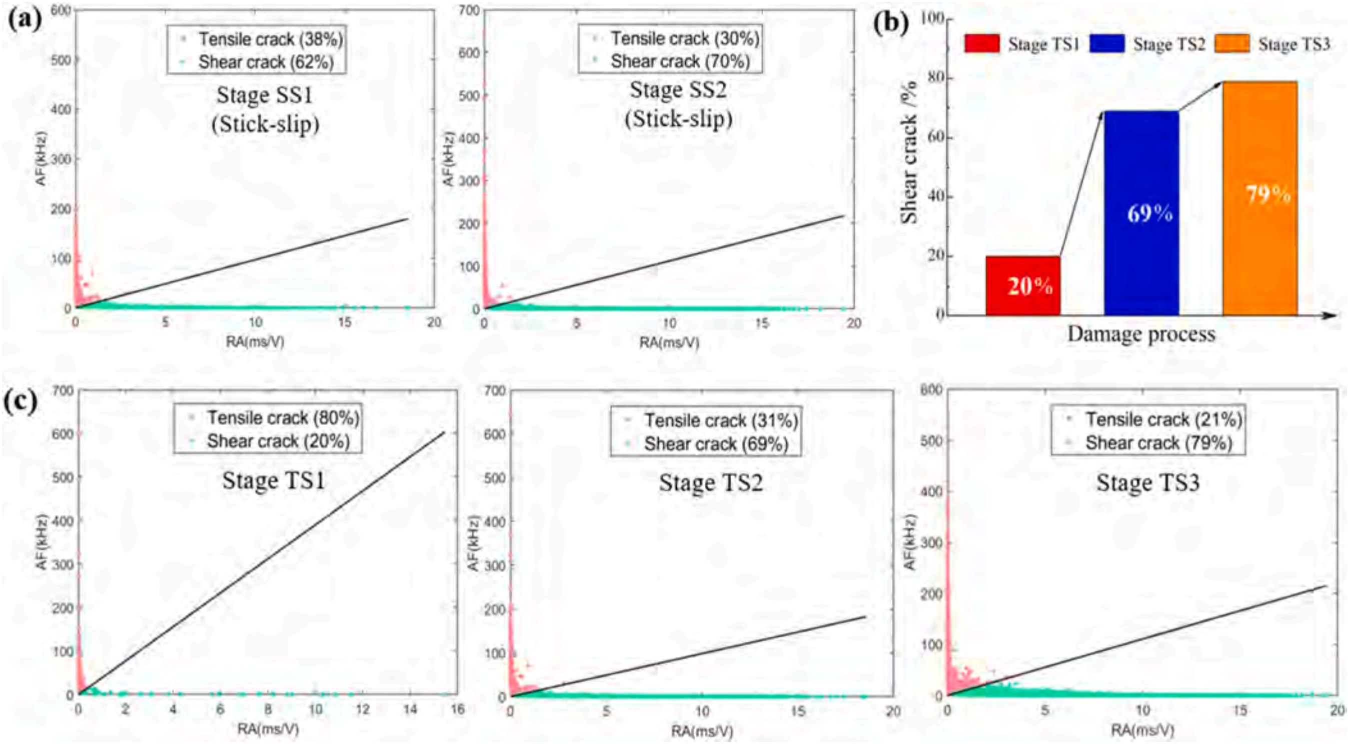

Fig. 13. Mode I and Mode II crack openings during the damage process: (a) results for two stick-slip stages; (b,c) results for three different damage stages.

The identified low-entropy regime (grey region) corresponds precisely to the critical zone determined via natural time analysis. Beyond this region, entropy increases sharply, reflecting the highly disordered post-critical state as localized fracture signals and plastic deformation dominate.

The entropy minimum at approximately 65% of the normalised time signifies the transition from a disordered, multi-scale damage regime to an ordered, correlated regime that governs the subsequent failure process. In the disordered regime, microcracks nucleate independently across the beam. In the ordered regime, a dominant damage mechanism takes control, specifically interfacial debonding followed by transverse shear cracking. This low-entropy state represents the information-theoretic manifestation of the system approaching a critical point, thereby complementing the natural time and MCF-B analyses.

5.7. MCF-B analysis: Beyond the b-value

The MCF-B method addresses limitations of classical *b*-value analysis by introducing dual exponents. Fig. 15c presents the evolution of p_2 (power-law exponent) and p_3 (exponential exponent) throughout loading. Criticality is identified by a characteristic two-stage signature: first, the presence of a perfect power law with $p_2 > 1$ and $p_3 \approx 0$, followed by a decrease in p_2 accompanied by a monotonic increase in p_3. This crossover phenomenon, indicated by the black dotted box in Fig. 15c, signals the approach to failure. Notably, the critical region identified by MCF-B aligns with that from natural time analysis and AE entropy—three independent methods converging on the same physical state.

Fig. 16 directly compares MCF-B results with traditional *b*-value analysis. While the *b*-value decreases approaching the critical region (consistent with expectations), it exhibits divergent trends thereafter. In

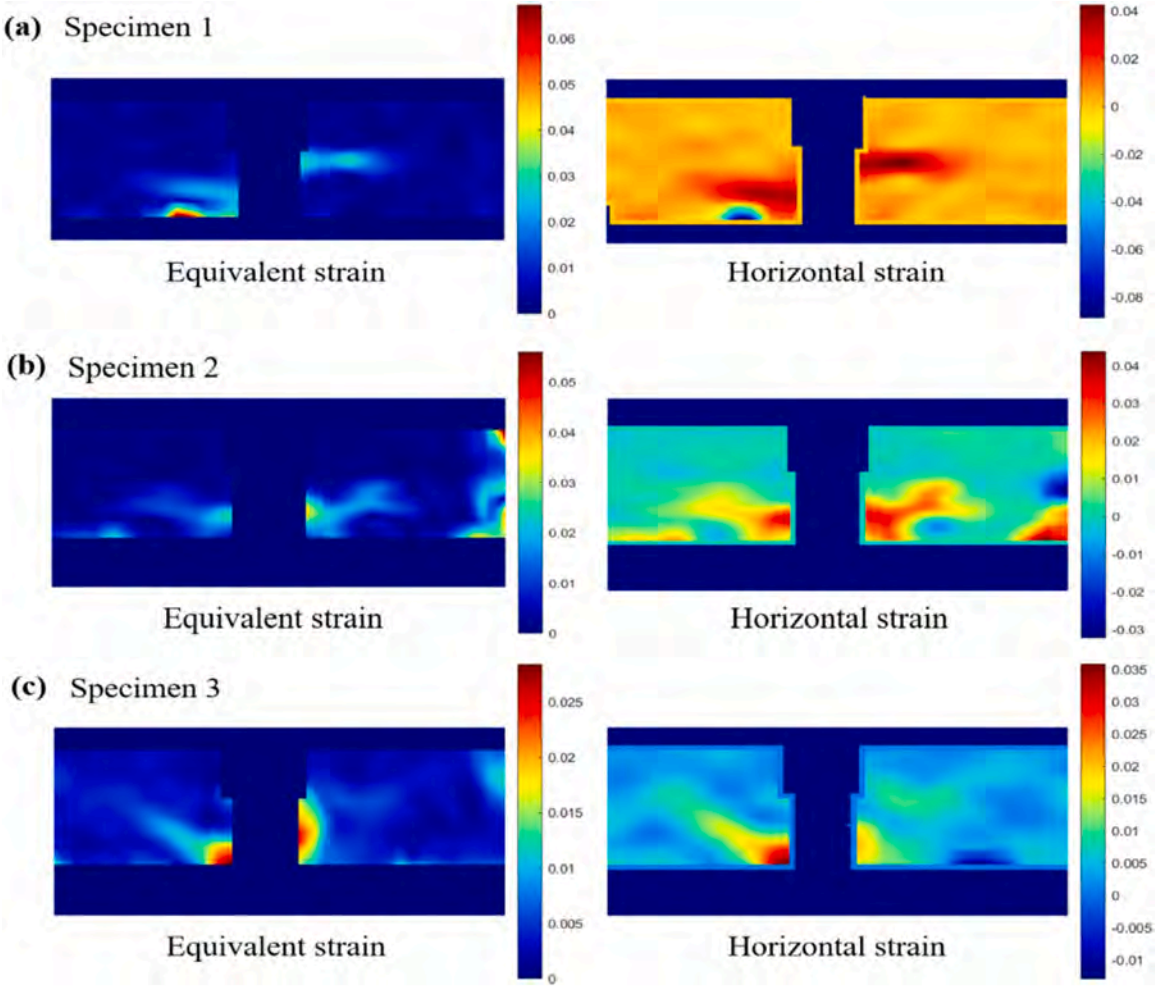

Fig. 14. DIC strain field diagram at the final failure for GFRP-bar reinforced concrete beams.

contrast, MCF-B maintains its critical signature through the systematic crossover behaviour.

This comparison highlights the robustness of the MCF-B approach: by accounting for deviations from pure power-law behaviour through the dual-exponent formulation, it captures the final approach to failure even when the *b*-value loses its precursory signature.

5.8. *Synthesis of damage process*

The multi-technical analysis enables a comprehensive description of the damage process in GFRP-bar reinforced concrete across four distinct phases. In the initial stage (TS1), distributed microcracking with tensile dominance is observed, characterized by stable AE activity, high *b*-values, and moderate entropy. During the subsequent stick-slip phase (TS2), intermittent bond failure generates a saw-tooth load response, with each slip signal producing a corresponding AE burst, while RA-AF analysis reveals a distinct transition toward shear-dominated cracking. As the structure approaches a critical transition at approximately 0.65 normalized time, multiple independent indicators converge: natural time variance approaches the critical value of 0.07, entropy reaches its minimum, and the MCF-B method exhibits crossover behaviour, signalling that the system has entered a correlated damage state. In the final failure stage (TS3), shear cracks predominate at a ratio of approximately 4:1 relative to tensile cracks, and transverse shear cracks propagate near the GFRP bar, ultimately leading to pull-out failure. This progression, captured in real time by AE and validated by DIC and mechanical measurements, demonstrates the power of integrated multi-technical monitoring, while reinforcing the consistency of AE-based damage indicators across scales.

6. Structural scale: from laboratory to field applications

6.1. *Case study I: UHPC strengthening of long-term damaged RC beams*

6.1.1. *Unique experimental context*

The beams in this study represent a unique experimental resource: RC notched beams subjected to 24 years of sustained loading in a controlled basement environment (1998–2022). This long-term loading created a realistic pre-damaged state, including creep deformation, microcrack networks, and stress redistribution, that cannot be replicated through short-term pre-damage protocols.

Fig. 17 illustrates the sustained loading setup, with each beam subjected to four-point bending via hanging weights. The notched configuration (60 mm and 90 mm notch depths) created distinct initial fracture process zones for subsequent UHPC strengthening.

6.1.2. *Characterization of pre-damage state*

After 24 years of sustained loading, comprehensive characterization of the beams revealed the pre-damage state across multiple aspects. Regarding deflection development, the R90 beam (with a 90 mm notch) exhibited significantly larger long-term deflections than the R60 beam, reflecting greater initial section loss and accelerated creep, as shown in Fig. 18. Crack patterns were found to distribute regularly near the stirrups, reflecting stress concentrations at these locations; these pre-

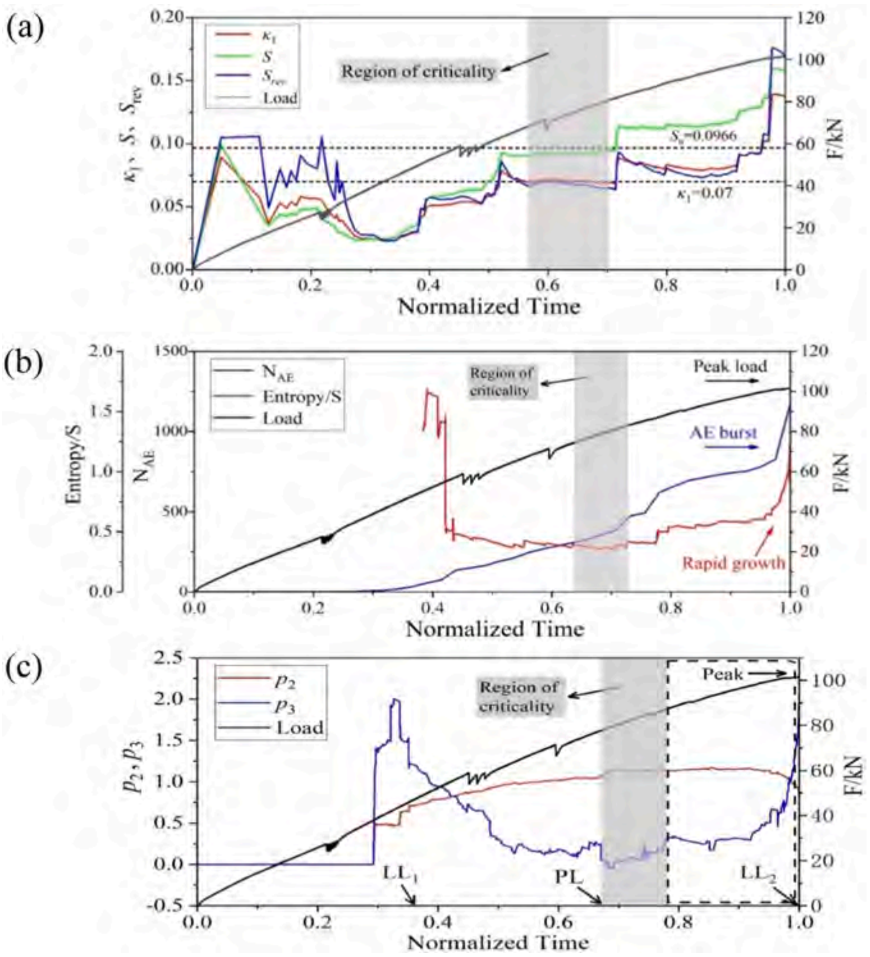

Fig. 15. Multi-technique criticality indicators: (a) natural time analysis; (b) AE entropy analysis; (c) MCF-B analysis. Grey background indicates consistent critical region identified by all methods.

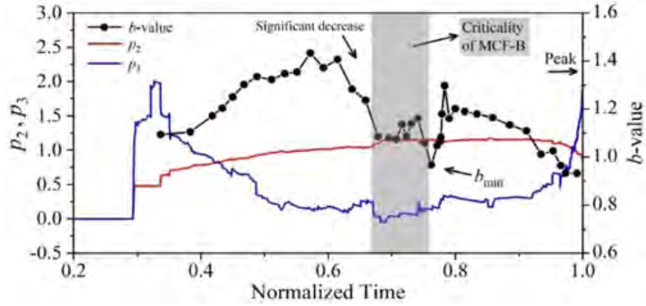

Fig. 16. Comparison of *b*-value and MCF-B analysis. Grey area indicates MCF-B critical region.

existing cracks served as initial flaws that would subsequently influence post-strengthening fracture behaviour. Carbonation depth measurements indicated a maximum carbonation depth of 10.1 mm, which remained well below the 25 mm concrete cover, confirming that chemical deterioration was minimal. Reinforcement corrosion analysis, presented in Table 3, revealed minimal mass loss, with a maximum of 2.47% for stirrups, confirming that mechanical damage rather than chemical degradation dominated the pre-damage state.

This pre-damage characterization established that the substrate deterioration was predominantly mechanical (creep and microcracking) rather than chemical, providing a realistic foundation for evaluating UHPC strengthening effectiveness.

6.1.3. *UHPC strengthening and mechanical response*

After 24 years, the beams were strengthened by filling notches with UHPC (2% steel fibre volume fraction) and tested to failure under four-point bending. Four AE sensors were fixed to each UHPC-reinforced beam (named U60 and U90) using high-vacuum grease, as illustrated in Fig. 19. Fig. 20 presents load-deflection responses, with the key parameters summarized in Table 4.

The U90 beam with a deeper UHPC layer exhibited an 18% higher ductility coefficient (5.2 vs. 4.4) despite a lower ultimate load, demonstrating that increased UHPC depth enhances deformation capacity, a critical consideration for seismic applications and damage tolerance.

6.1.4. *Failure modes and interfacial behaviour*

The failure patterns of the two UHPC-strengthened beams are illustrated in Fig. 21, revealing both common features and distinct differences. In both beams, the UHPC-RC vertical interface experienced delamination, while the horizontal interface remained intact throughout testing. However, key differences emerged between the two strengthening configurations. For the U60 beam, the primary flexural crack penetrated the horizontal interface and propagated into the RC layer, while separation at the left vertical interface induced significant diagonal cracks that extended toward the loading point. In contrast, for the U90 beam, flexural cracks were largely contained within the UHPC layer without penetrating the horizontal interface. Oblique cracks initiated at the vertical interface, extended to the horizontal interface, and then propagated toward the loading point, with additional cracking developing at the corners of the horizontal interface.

The failure was primarily governed by oblique cracking, with the

UHPC-RC interface playing a dominant role. The deeper UHPC layer in U90 resulted in longer vertical interfaces on both sides, delaying crack development and promoting more ductile response.

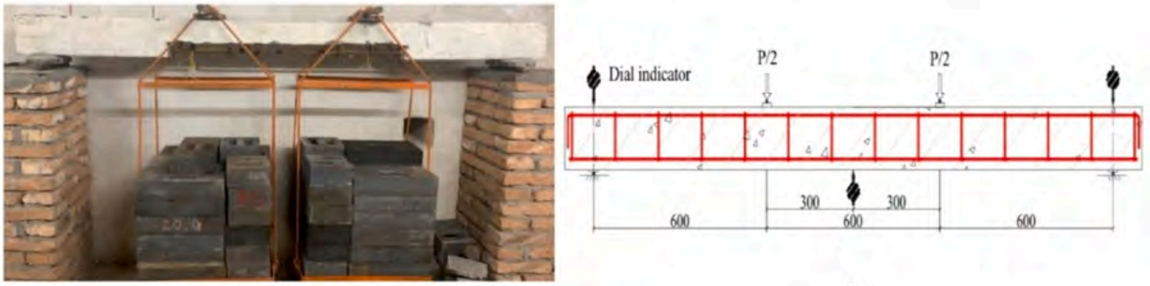

(a) (b)

Fig. 17. Test setup of long-term loaded RC notched beams: (a) site layout; (b) loading diagram (mm).

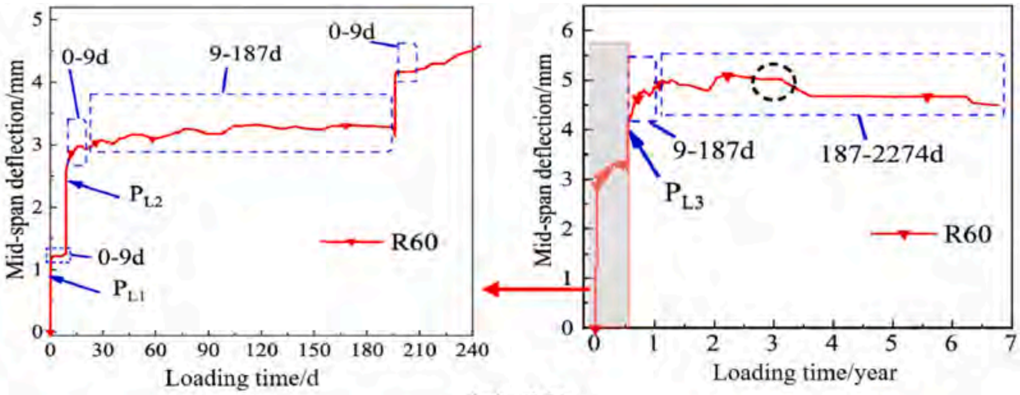

(a) R60

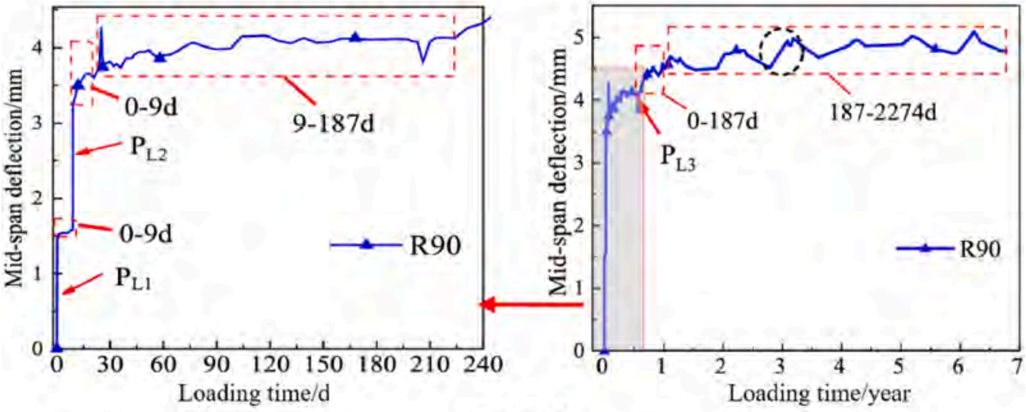

(b) R90

Fig. 18. Long-term deflection development under sustained loading.

Table 3
Steel rebar corrosion at notch of notched beams.

Type	Original weight/ g	Weight after cleaning/ g	Average mass loss
R60 steel rebars	65.518	64.531	1.51%
R90 steel rebars	60.967	60.284	1.12%
R60 stirrups	85.859	83.737	2.47%
R90 stirrups	97.876	96.118	1.80%

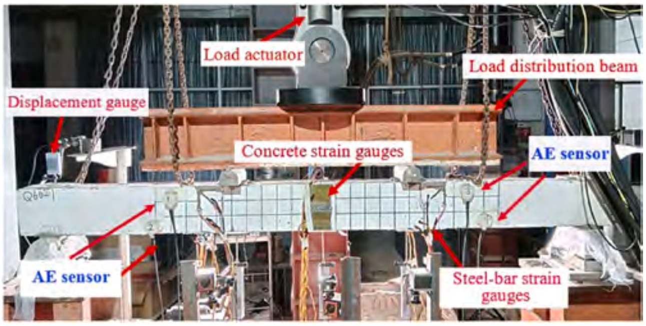

Fig. 19. Schematic of the test setup and AE sensor arrangement.

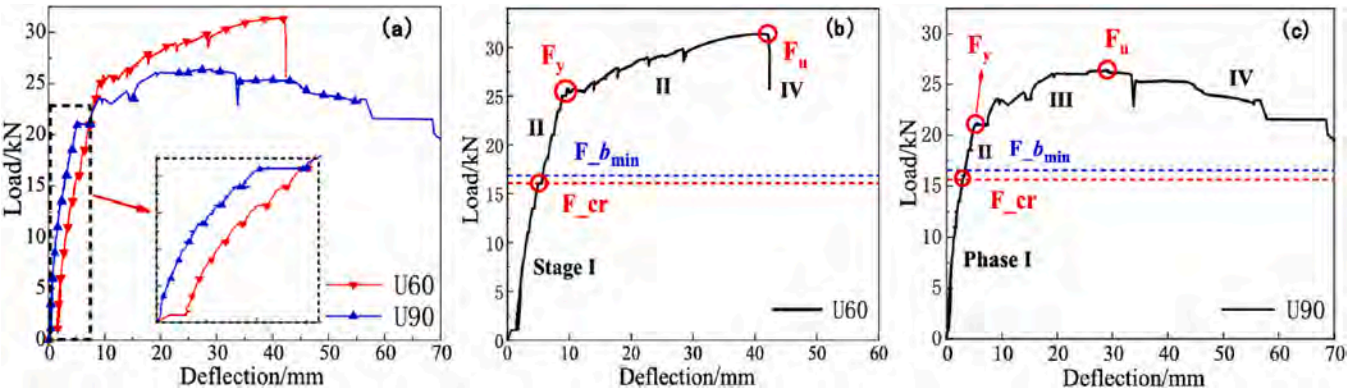

Fig. 20. Load-deflection curves for UHPC-strengthened beams.

Table 4
Main load-deflection values and ductility.

Beam	First fracturing load F_cr (kN)	Steel-rebar yield load F_y (kN)	Ultimate load F_u (kN)	Deflection at yield load Δy (mm)	Ultimate deflection Δu (mm)	Ductility coefficient μ= Δu / Δy
U60	16.4	25.4	31.4	9.6	42.1	4.4
U90	15.9	21.2	26.4	5.6	29.2	5.2

(a) U60

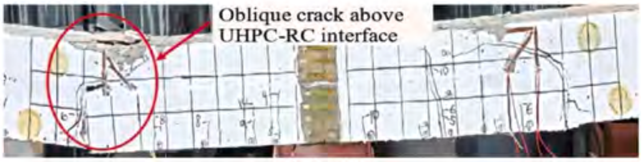

(b) U90

Fig. 21. Beam failure patterns for (a) U60 and (b) U90.

6.1.5. AE monitoring of damage evolution

AE monitoring provided real-time insight into the fracture process. Fig. 22 presents β_t and *b*-value evolution for both beams.

The U60 beam exhibited declining *b*-value regression (from 1.5 toward 1), revealing unstable crack propagation. The critical point occurred at 42 min (t_b_{min}), with $b_{\text{min}} = 0.9$ and $\beta_t = 1.2$ (>1), corresponding to initiation of flexural main cracks at beam bottom. In contrast, the U90 beam demonstrated relatively stable crack growth with nearly constant *b*-values. The critical point at 39 min ($b_{\text{min}} = 1.0$, $\beta_t = 2.5$) corresponded to vertical interface cracking, a less critical signal than main flexural cracking. As summarised in Table 5, the β_t and *b*-value results align well with the loading history, where t_b_{min} accurately identifies the initial fracturing point in the beams.

6.1.6. Natural time analysis validation

Natural time analysis identified critical points (t_{crit}) for both beams, consistently preceding *t_b*$_{\text{min}}$ by 2–3% (Table 6 and Fig. 23). This consistency validates both methods while demonstrating that natural time analysis provides earlier warning.

Table 5
Comparison of first fracturing load.

Strengthened beam	Loading history F_cr (kN)	*b*-value F_b_{min} (kN)	Deviation
U60	16.4	16.7	1.8%
U90	15.9	16.1	1.3%

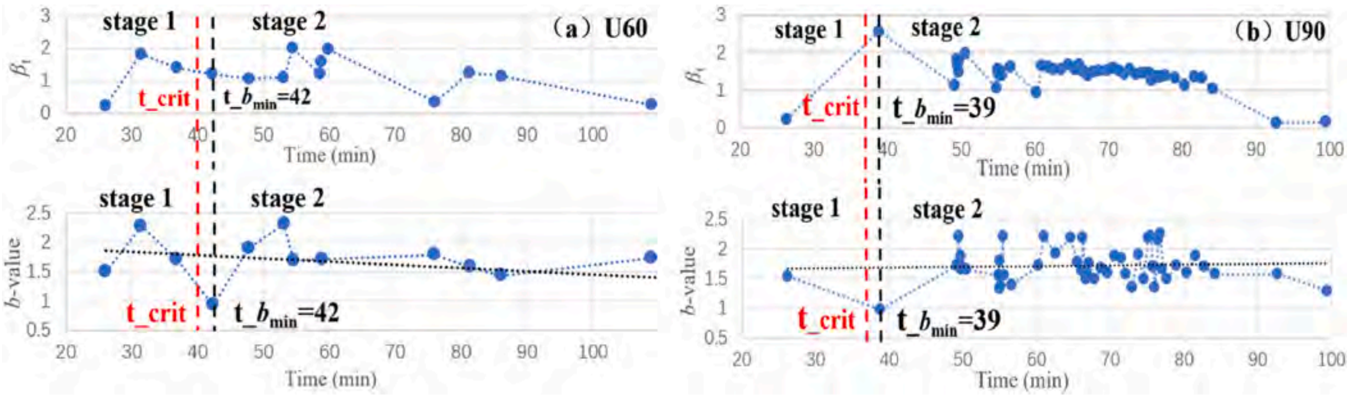

Fig. 22. AE β_t and *b*-value for (a) U60 and (b) U90 beams. t_{crit} determined using natural time analysis.

Table 6
Comparison between natural time and *b*-value.

AE analysis method	Time of first fracturing (minutes)	
	U60	U90
b-value (t_$b_{\min}$)	42	39
Natural time (t_crit)	41	38
Deviation	2.3%	2.5%

6.1.7. RA-AF analysis: fracture mode transition

RA-AF analysis, presented in Figs. 24 and 25, revealed distinct cracking patterns between the two beams. During the first stage of loading, shear cracks dominated in both strengthening configurations. However, a notable divergence emerged in the second stage: the U90 beam, which featured a deeper UHPC layer, exhibited a clear transition to tensile-dominated cracking, reflecting the enhanced ductility conferred by the increased UHPC depth. In contrast, the U60 beam maintained shear-dominated cracking throughout this stage, underscoring the role of UHPC thickness in promoting a more favourable fracture mode.

The proportion of tensile cracks in U90 increased by approximately 25% in the final failure stage compared to U60, confirming the transition to a more ductile fracture mode. This shift from Mode II to Mode I fracture represents a fundamental change in energy dissipation mechanism.

It is acknowledged that AE alone cannot unambiguously distinguish newly formed cracks from the reactivation of 24-year-old microcracks. However, the pre-damaged state, characterised by a distributed microcrack network with minimal corrosion, serves as an initial fracture process zone. The value of AE monitoring lies not in retrospective classification of crack age but in real-time assessment of the post-strengthening structural response, including the transition from distributed to localised damage and the shift in dominant fracture mode.

6.1.8. Synthesis: Fracture mechanics interpretation

The long-term pre-damage created distinct initial conditions for the two beams, with the deeper notch in R90 resulting in greater loss of flexural stiffness, higher stress levels in the tensile reinforcement, and accelerated microcrack development compared to the R60 beam. Following UHPC strengthening, this pre-damaged state influenced post-strengthening fracture behaviour through several interconnected mechanisms. First, the pre-existing microcrack network served as an initial fracture process zone, directly influencing subsequent crack propagation paths. Second, the vertical UHPC-RC interface acted as a pre-defined plane of weakness where stress concentration concentrated,

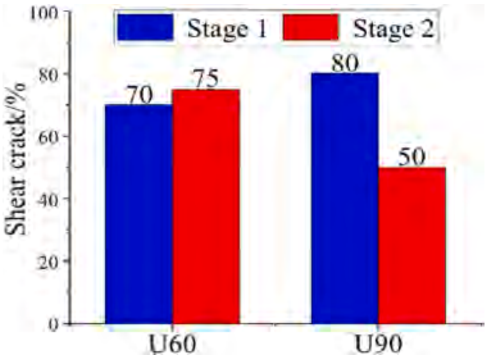

Fig. 25. Crack ratios at different stages.

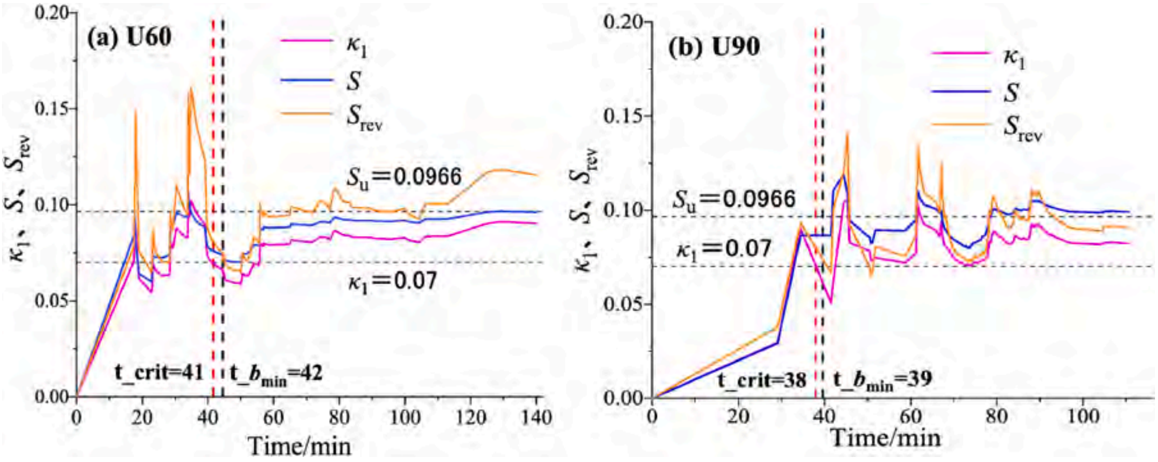

Fig. 23. AE natural-time analysis for (a) U60 and (b) U90 beams.

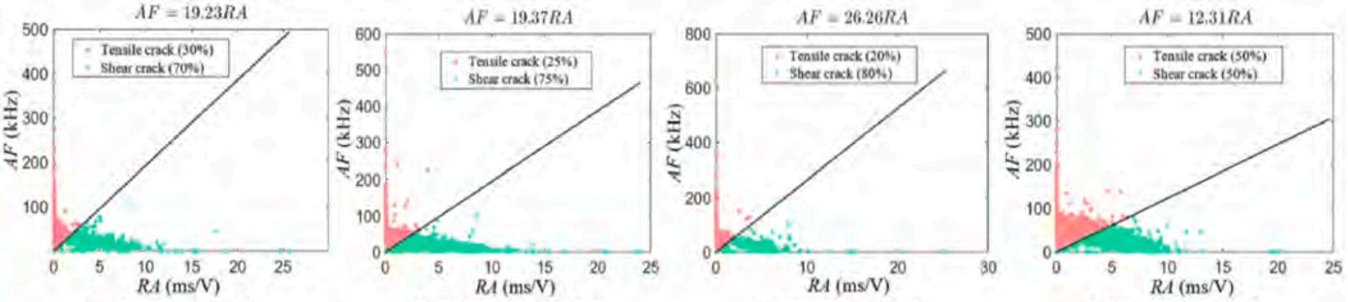

(a) U60 stage 1 (b) U60 stage 2 (c) U90 stage 1 (d) U90 stage 2

Fig. 24. RA and AF analysis for U60 and U90 beams.

leading to critical crack initiation. Third, the steel fibres embedded in the UHPC provided a cohesive zone ahead of crack tips, significantly increasing the effective fracture energy of composite system. Finally, despite the development of cracking, the neutral axis depth remained remarkably stable throughout loading, as shown in Fig. 26, representing a macro-scale manifestation of UHPC's enhanced fracture toughness.

The integration of AE monitoring within a fracture mechanics framework provided unprecedented insight into these mechanisms, demonstrating that AE parameters directly reflect the energy release processes during crack propagation across scales.

6.2. *Case study II: field monitoring of UHPC bridge deck cracking*

6.2.1. *Context and challenge*

The Niutianyang Bridge in Shantou, China, is a long-span cable-stayed bridge with a main span of 468 m, as shown in Fig. 27. The orthotropic steel deck is composited with a 50 mm UHPC layer overlaid with 40 mm asphalt wearing course. During construction, drying shrinkage cracks were observed on the UHPC deck layer at the main span centre, representing a critical concern for long-term durability. It is important to note that the AE monitoring campaign was focused exclusively on this local cracked region at the midspan of the deck, not on the entire 468 m bridge span.

This field case represents the ultimate scale in the multi-scale progression: from material (UHPC properties), through element (composite deck behaviour), to full structure (cable-stayed bridge response). The challenge was to monitor crack evolution in real time under construction conditions, with traffic loading and environmental effects.

In this field study, because four sensors were used and source localization was performed via triangulation, the term ‘AE event’ is used to denote a group of AE signals originating from a common physical crack source.

6.2.2. *Field AE monitoring setup*

The monitoring targeted the identified cracked zone on the UHPC deck layer at the main span centre. Within this local region, four AE sensors were strategically placed near the observed cracks (Fig. 28). The ÆMISSION® wireless system enabled real-time data transmission to a remote server. Threshold settings (2 mV) and frequency filtering (>20 kHz) were established based on pre-test background noise characterization, achieving 99% noise suppression while retaining 92% of crack-related signals.

The threshold was set at 2 mV based on pre-test background noise characterisation and remained fixed throughout the monitoring period to avoid desensitisation during high-traffic periods. The reported 99% noise suppression rate was obtained from laboratory validation tests using pre-recorded field noise, not from online adaptive filtering. This conservative strategy prioritises detection sensitivity over false-alarm minimisation, with subsequent correlation analysis (Section 6.2.6) used to identify traffic-related AE activity.

6.2.3. *AE time series analysis*

Fig. 29 presents the AE results recorded over a 225-minute monitoring period on October 23, 2023, during which two main AE events were identified. The first event occurred at the 73rd minute, characterized by a sharp acceleration in AE activity reaching 60 signals per minute. A second, sub-sharp acceleration followed at the 183rd minute, with AE activity peaking at 30 signals per minute. These two events marked critical moments of crack propagation in the UHPC deck layer.

The evolution of the β_t coefficient and b-value provided quantitative signatures of the damage progression throughout the monitoring period. During the initial period from 0 to 50 min, the β_t coefficient remained approximately 0.5 while the b-value ranged between 1.4 and 1.5, indicating a microcracking regime characterized by distributed damage. At the 73rd minute, coinciding with the first major AE event, the β_t coefficient increased sharply to 1.5 while the b-value decreased to approximately 1.0, signalling the transition to unstable crack evolution. A similar pattern was repeated at the 183rd minute, where the β_t coefficient again showed an abrupt increase and the b-value approached the critical threshold of 1.0, confirming the occurrence of a second episode of macrocrack propagation.

The two main AE events corresponded to macro-crack propagation, with b-values approaching 1.0, the critical threshold for macrocrack formation identified in material and element-scale studies.

6.2.4. *Correlation with field crack measurements*

Crack width and length were measured manually every 20 min (Fig. 30). The two major jumps in measured crack dimensions occurred precisely at the times of the two main AE events, confirming strong temporal correlation. Moreover, the magnitude of AE increase correlated with the magnitude of crack jump.

6.2.5. *AE source localization*

Triangulation based on arrival time differences located AE sources (red dots in Fig. 31), tracing crack tip advancement. The two more widely spaced AE sources represented the two main events at 73 and 183 min, signalling rapid crack tip advancements. The step-by-step upward progression of red dots matched the measured crack propagation pattern.

6.2.6. *Environmental and traffic effects*

Analysis of potential triggers for the observed AE activity revealed

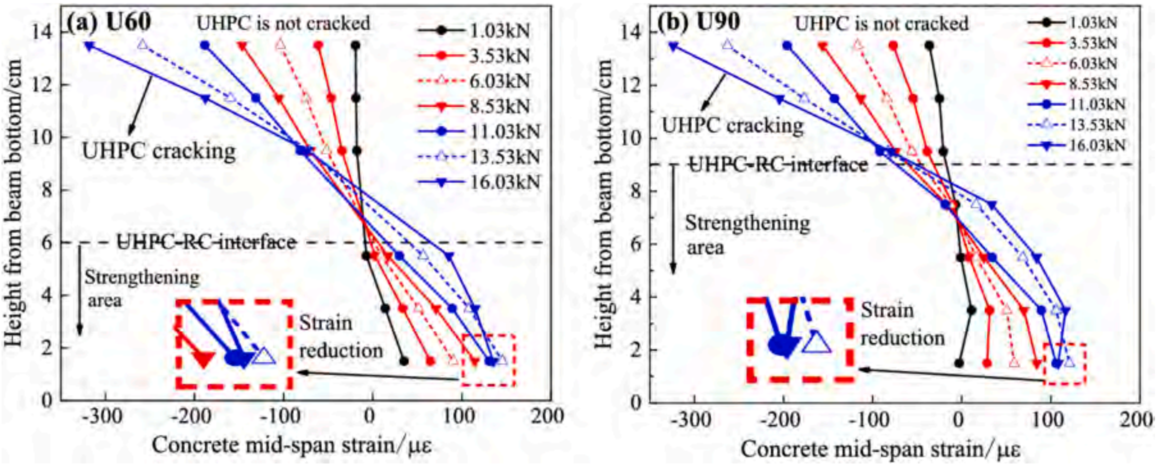

Fig. 26. Height-strain curves of midspan concrete.

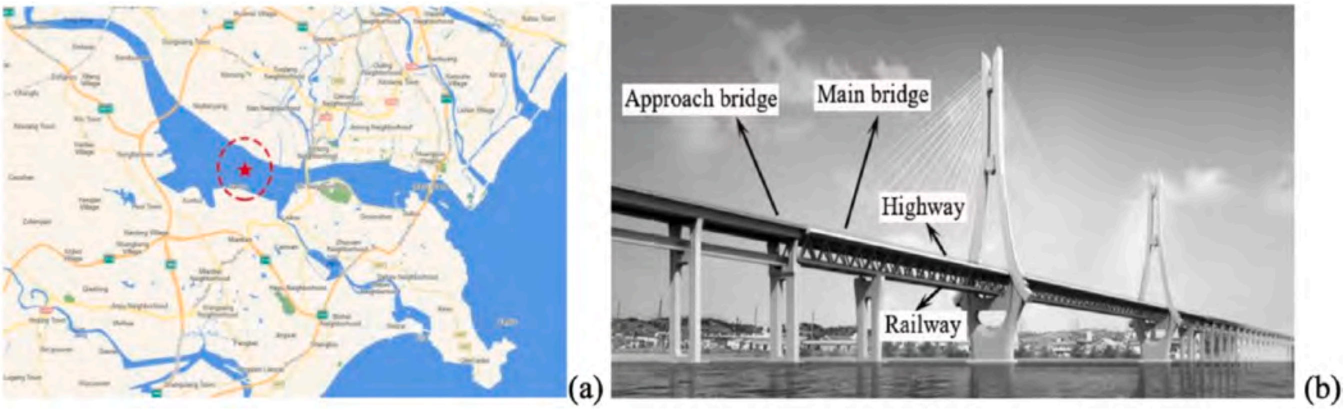

Fig. 27. The monitored bridge: (a) localization on map; (b) bridge photo.

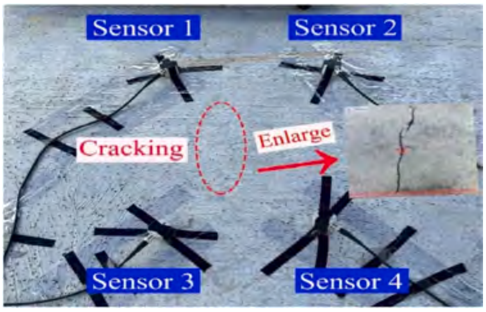

Fig. 28. Layout of AE sensors on the local cracked region of UHPC deck layer.

distinct contributions from environmental and operational sources. Regarding earthquake effects, a magnitude 5.0 earthquake occurred locally at 03:20 on the monitoring day; however, as shown in Fig. 32a, no statistical correlation was found between subsequent aftershocks and AE activity, indicating that seismic events did not contribute meaningfully to the observed crack propagation. In contrast, traffic effects exhibited a strong correlation with AE events, as illustrated in Fig. 32b. Cumulated AE curves grew rapidly immediately following peaks in construction vehicle traffic, confirming that vehicle loading was the primary driver of crack propagation in the UHPC deck layer during the monitoring period. Temperature effects may have contributed through thermal contraction of the main girder, producing tensile stress that exacerbated crack opening.

6.2.7. *Implications for structural monitoring*

This field case validated several principles previously established in laboratory studies, demonstrating the robustness and scalability of AE-based damage assessment. First, the *b*-value was confirmed as a reliable failure precursor, with its decrease to approximately 1.0 signalling macrocrack propagation in the bridge deck, a finding consistent with observations at both material and element scales. Second, the β_t coefficient served as an effective instability indicator, with values exceeding 1.0 coinciding with unstable crack evolution, matching laboratory findings from controlled testing. Third, triangulation techniques for AE source location successfully tracked crack tip advancement in a real structure, demonstrating the practical applicability of localization methods beyond laboratory conditions. Most significantly, the multi-scale consistency of AE parameters was confirmed: the same indicators that characterized microcracking in 75 mm laboratory specimens provided early warning of cracking in a 468 m bridge span, underscoring the scale-invariant nature of AE as a damage monitoring tool.

7. Unified discussion: cross-scale synthesis

7.1. *Common patterns across scales*

The four studies, spanning six orders of magnitude in characteristic dimension (from 75 mm specimens to 468 m bridge spans), reveal remarkable consistency in damage evolution patterns. Table 7 synthesizes key observations across scales.

Several universal patterns emerge from the cross-scale synthesis, revealing fundamental characteristics of damage evolution that persist across vastly different structural scales. The *b*-value functions as a universal precursor, with its decrease to approximately 1.0 reliably signalling the transition from distributed microcracking to localized macrocrack propagation across all investigated scales; this threshold appears scale-invariant, providing a robust indicator independent of specimen size or structural configuration. The invariance of the *b*-value threshold near 1.0 has been extensively documented in both laboratory-scale acoustic emission studies and geophysical seismology, demonstrating that the transition from criticality to final collapse follows consistent statistical laws across scales [39,54]. Furthermore, the convergence of natural time variance κ_1 to the critical value of 0.07 is rooted in the physical foundations of Natural Time Analysis, which applies uniformly from earthquake-scale phenomena to laboratory-scale fracture, representing a genuine physical law rather than an empirical observation [41–45]. The β_t coefficient serves as a consistent instability indicator, with values exceeding 1.0 consistently accompanying unstable crack propagation whether observed in laboratory snap-back instabilities or field crack jumps. Fracture mode transitions exhibit systematic patterns that reflect the influence of reinforcement and interfaces on damage evolution, as demonstrated by the progression from tensile to shear cracking in GFRP beams and the reverse transition from shear to tensile cracking in UHPC-strengthened beams. Finally, the correlation between AE activity and fracture events proves remarkably consistent: every significant mechanical event, including load drops, snap-back instabilities, and crack jumps, produces a corresponding AE burst, validating AE as a direct quantitative measure of dynamic fracture energy release.

7.2. *The unifying role of fracture mechanics*

Fracture mechanics provides the theoretical framework that unifies observations across scales. The fracture process zone, which in concrete spans multiple aggregate sizes, scales with structure size while maintaining similar local energy dissipation mechanisms [58]. This scaling property explains why AE parameters remain meaningful indicators regardless of structure size.

The energy balance perspective is particularly illuminating. The total energy released during fracture, R, partitions into dissipated energy D

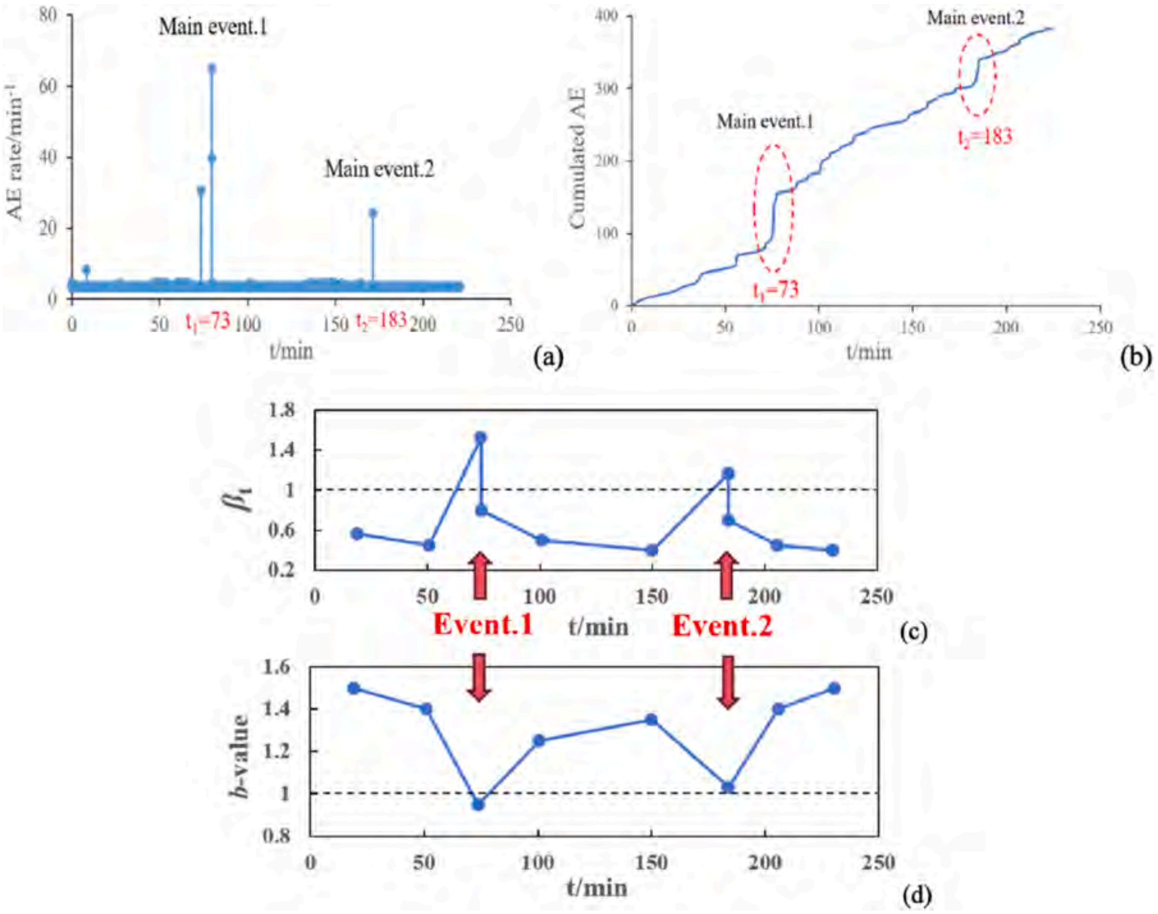

Fig. 29. AE time series results: (a) AE count rate; (b) cumulated AE; (c,d) β_t and *b*-value.

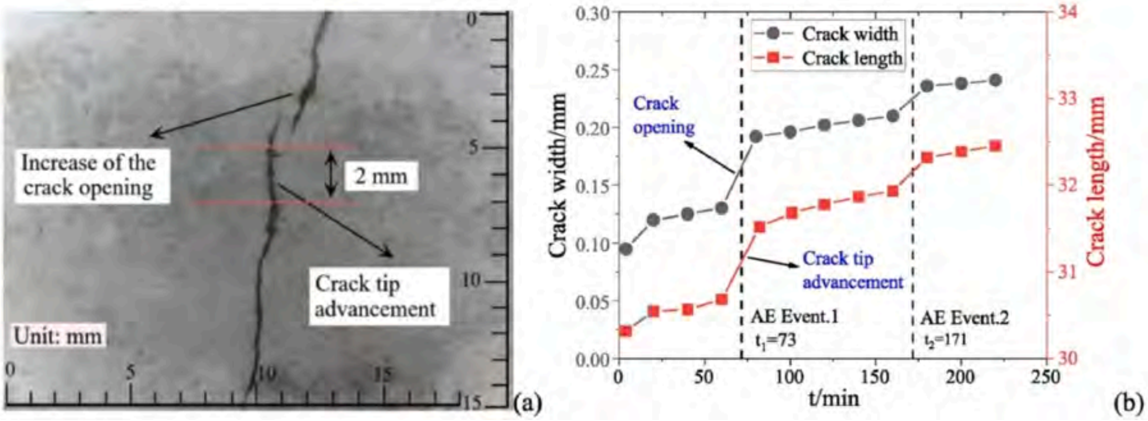

Fig. 30. Crack curve measured in the field.

and emitted energy E (detected as AE). The correlation between load drops and AE bursts observed in all studies confirms that a significant fraction of the dynamic energy release during unstable crack propagation is captured by AE monitoring.

Furthermore, the fractal analysis from material-scale studies, which yielded a fractal dimension D = 2.19, has profound implications for structural monitoring: damage localizes on surfaces rather than volumes. This explains why AE sensors placed on structural surfaces can effectively monitor internal crack propagation, as the fracture process concentrates near the surface where sensors are located.

7.3. *Methodological advances*

The progression from simple *b*-value analysis to multi-technical approaches represents a significant methodological advance:

RA-AF analysis moves beyond scalar damage quantification to identify fracture modes. The consistent observation of mode transitions, from tensile to shear in GFRP beams and from shear to tensile in UHPC-strengthened beams, demonstrates that fracture mechanisms evolve in characteristic ways that can be tracked in real time.

Natural time analysis provides earlier warning than conventional methods by detecting critical state transitions before macroscopic

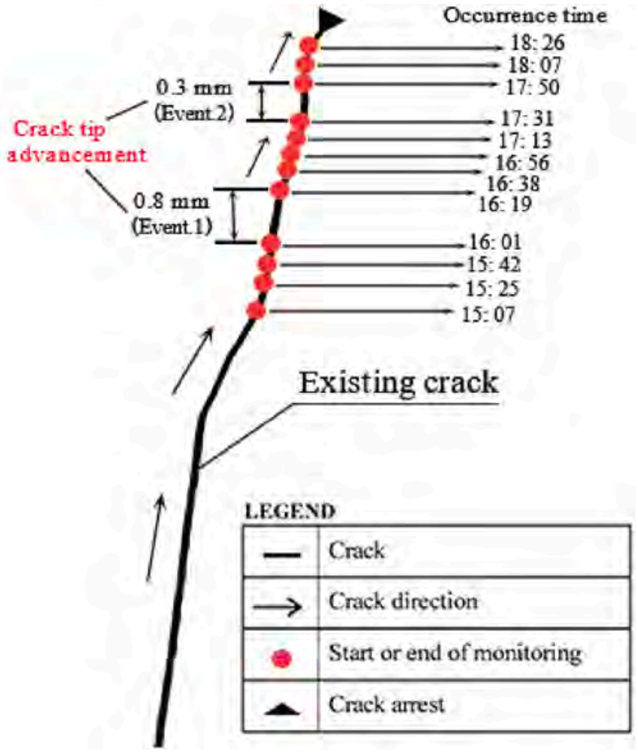

Fig. 31. Crack tip advancement trace positioned by AE sources (red points).

failure. The consistent observation that natural time critical points precede *b*-value minima (by 2–3% in all studies) establishes this method as a valuable complement to traditional analysis.

AE entropy offers a measure of system order that peaks at critical transitions. The convergence of entropy minima with natural time critical points demonstrates that different physical descriptors, specifically temporal correlation and statistical disorder, point to the same underlying physical state.

MCF-B analysis addresses limitations of classical *b*-value by capturing deviations from pure power-law behaviour. The superior performance of MCF-B in maintaining critical signature beyond the point where *b*-value diverges suggests this method may be particularly valuable for complex systems where multiple damage mechanisms coexist.

7.4. Implications for structural health monitoring

The cross-scale synthesis yields several direct implications for practical structural health monitoring. For early warning systems, the consistent behaviour of AE parameters prior to critical events provides a robust basis for automated alert mechanisms. Thresholds established under controlled laboratory conditions, specifically *b*-value below 1.1, β_t coefficient exceeding 1.0, and natural time variance approaching 0.07, can be applied to field monitoring with appropriate calibration for site-specific conditions. Regarding damage localization, source localization techniques validated in the bridge deck study demonstrated the capability to locate active cracks in real time, enabling targeted inspection and repair; the quadrilateral sensor array achieved sufficient accuracy for practical applications despite the challenging conditions inherent to field environments. For performance validation, AE monitoring provides objective measures of strengthening effectiveness, as demonstrated in the UHPC-strengthened beams where stable *b*-values and tensile-dominated cracking in the U90 beam confirmed improved ductility and validated the deeper UHPC application. Finally, for remaining life assessment, the identification of critical states does not imply imminent failure, as the GFRP beams sustained significant additional loading after the critical region, but rather marks the onset of the terminal phase during which damage processes become correlated and the risk of global failure increases substantially.

7.5. Limitations and future directions

Several limitations of the current research should be acknowledged to guide future developments. Regarding sensor configuration, laboratory studies typically employed only one to two sensors, which inherently limited source localization capability, while the field study utilized four sensors to achieve localization but with finite accuracy; future work

Table 7
Cross-scale synthesis of damage evolution patterns.

Scale	Specimen/ Structure	Dominant Fracture Mode	AE-Fracture Correlation
Material	Plain concrete cubes	Crushing-to-cracking transition	Each snap-back → AE burst
Element	GFRP-RC beams	Tensile-to-shear transition (RA-AF)	Each load drop → AE peak
Structure I	UHPC-strengthened beams	Shear-to-tensile (deeper UHPC)	AE bursts at yield and ultimate
Structure II	UHPC bridge deck	Transverse cracking	AE events match measured crack jumps

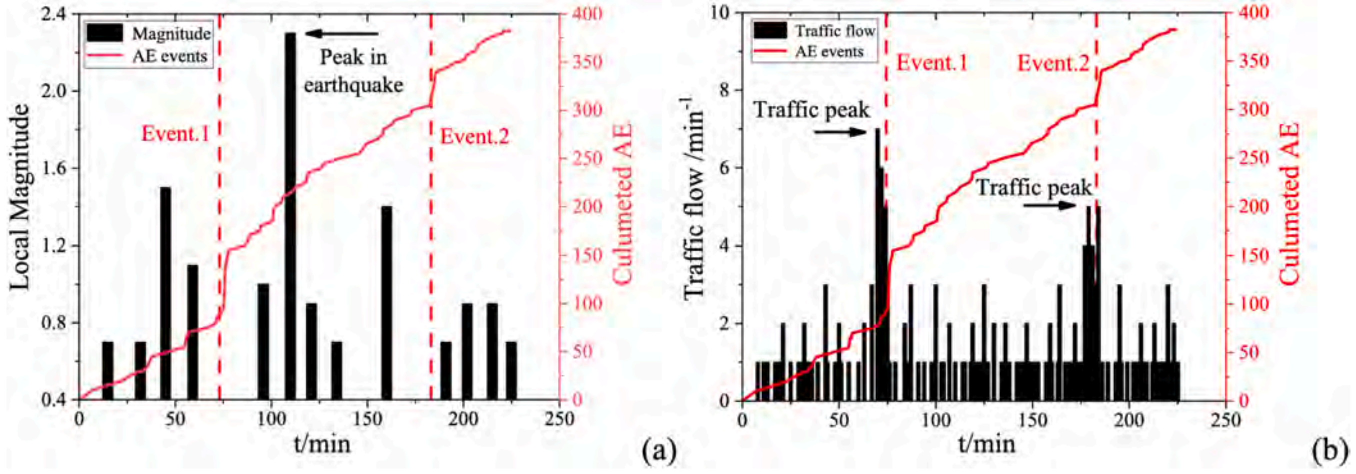

Fig. 32. Analysis of AE and environmental effects: (a) AE and earthquakes; (b) AE and vehicle traffic.

should employ denser sensor arrays to improve spatial resolution. Material specificity represents another consideration, as the results presented are specific to concrete and cement-based materials; although the underlying principles likely extend to other quasi-brittle materials, validation for each new material class remains necessary. Environmental effects pose ongoing challenges, particularly in field monitoring where wind, traffic, and temperature variations introduce noise; while the filtering protocols employed proved effective, adaptive algorithms could further enhance signal-to-noise ratio. Data volume presents a practical constraint, as continuous monitoring generates massive datasets, necessitating the development of automated analysis algorithms for practical implementation.

While the preprocessing parameters and window sizes employed in this study were consistently applied across scales and shown to be stable through internal cross-consistency checks, a formal parametric sensitivity analysis with exhaustive variation of each parameter remains a valuable but resource-intensive effort for multi-scale AE datasets. Future work should systematically investigate adaptive thresholding, data-driven window optimization, and automated parameter selection to further enhance the robustness and transferability of AE-based damage indicators across different structural scales and field environments.

Looking forward, several promising directions emerge for advancing AE-based structural health monitoring. Integration with numerical models, such as coupling AE monitoring with discrete element or peridynamic simulations, could enable predictive assessments of remaining structural life based on observed damage states. Machine learning approaches offer the potential to identify damage signatures beyond human detection capabilities, potentially revealing earlier or more reliable precursors. Multi-physics monitoring, combining AE with complementary techniques including DIC, strain gauges, and thermography, provides redundancy and cross-validation essential for critical infrastructure applications. Finally, long-term validation through extended monitoring campaigns on in-service structures is needed to confirm that laboratory-identified precursors remain reliable over years and decades of service.

8. Conclusions and perspectives

This work presented a coherent body of original research unified by a common methodological framework: the integration of AE monitoring with complementary techniques to investigate damage and fracture processes across scales. From 75 mm concrete cubes to a 468 m cable-stayed bridge, the same physical principles govern damage evolution, and the same AE parameters provide reliable indicators of structural state.

The principal conclusions of this study are summarized as follows. Firstly, scale-invariant damage indicators, including *b*-value, β_t coefficient, natural time variance, and entropy, exhibited consistent behaviour at failure across six orders of magnitude in structural scale. Specifically, the decrease of the *b*-value to approximately 1.0 serves as a universal signal for the transition from distributed microcracking to localized macrocrack propagation. This observation is further supported by the fractal dimension of emitted energy ($D = 2.19$), which confirms that damage concentrates on preferential surfaces and validates surface-mounted AE monitoring as an effective approach for detecting internal crack growth. Furthermore, RA-AF analysis revealed characteristic transitions between tensile and shear cracking modes preceding failure, providing critical insights into changing energy dissipation mechanisms. By employing natural time analysis and MCF-B methods, critical states were identified prior to macroscopic failure, offering earlier warnings than conventional analysis; the convergence of these independent methods on the same critical region provides robust evidence for the underlying physical transitions. Finally, the practical applicability of these laboratory-identified precursors was validated through field monitoring of a UHPC bridge deck, where AE successfully tracked crack evolution and located active tips. In practical reinforcement scenarios, AE monitoring of 24-year pre-damaged beams strengthened with UHPC quantified a significant improvement in ductility, with an 18% increase observed for deeper UHPC applications, thereby providing quantitative guidance for future retrofit designs.

The progression from material to structure is not merely a change in specimen size but a continuous exploration of fracture phenomena that follow scale-invariant laws. AE, grounded in fracture mechanics and validated by multi-technical experimental evidence, provides a unique window into this multi-scale damage evolution. The principles established in this synthesis offer a foundation for the next generation of structural health monitoring systems, systems that not only detect damage but interpret its physical significance, predict remaining life, and guide intervention strategies.

As civil infrastructure ages worldwide and new materials enable unprecedented structural forms, the need for such physically grounded monitoring approaches will only grow. The integration of AE with complementary techniques, interpreted through fracture mechanics and validated across scales, provides a pathway toward structures that continuously assess their own health and communicate their condition to those responsible for their safety.

CRediT authorship contribution statement

Yang Yang: Methodology, Investigation, Conceptualization. **Zhiwen Zhu:** Methodology, Investigation, Data curation. **Zihan Jiang:** Writing – original draft, Validation, Methodology, Investigation, Formal analysis, Data curation. **Jueliang Chen:** Investigation, Conceptualization. **Giuseppe Lacidogna:** Writing – review & editing, Methodology, Investigation, Formal analysis, Conceptualization.

Declaration of Competing Interest

The authors declare that they have no known competing financial interests or personal relationships that could have appeared to influence the work reported in this paper.

Acknowledgments

The authors wish to acknowledge the China Scholarship Council (CSC) and the sponsorship guaranteed with basic research funds provided by Politecnico di Torino, Italy for their support in this work.

Data availability

Data will be made available on request.

References

[1] A. Carpinteri, G. Lacidogna, N. Pugno, Structural damage diagnosis and life-time assessment by acoustic emission monitoring, Eng. Fract. Mech. 74 (1-2) (2007) 273–289.
[2] Z.P. Bazant, J. Planas, Fracture and Size Effect in Concrete and Other Quasibrittle Materials, CRC Press, Boca Raton, FL, USA, 1998.
[3] C. Wang, S. Zhou, Z. Jiang, Z. Zhu, Multi-technology investigation on damage mechanisms in hybrid reinforced concrete beams: synergistic effects of reinforcement and fiber content, Constr. Build. Mater. 506 (2026) 144820.
[4] S. Zhou, Z. Jiang, Q. Ou, J. Liu, C. Wang, Analysis on flexural toughness of steel fiber reinforced concrete based on acoustic emission and digital image correlation techniques, Constr. Build. Mater. 492 (2025) 143039.
[5] C. Wang, Z. Jiang, F. Accornero, S. Zhou, Q. Ou, Influence of seawater and salt ions on the properties of calcium sulfoaluminate cement, J. Mater. Civ. Eng. 37 (6) (2024) 04025156.
[6] J.G.M. Van Mier, Fracture Processes of Concrete, CRC Press, Boca Raton, FL, USA, 2017.
[7] Z. Jiang, C. Li, G. Lacidogna, Crack propagation and intelligent prediction in asphalt pavements under moving loads, Int. J. Pavement Res. Technol. (2026) 1–16.
[8] B.L. Karihaloo, Fracture Mechanics and Structural Concrete, Longman, Harlow, UK, 1995.

[9] Z. Zhu, Z. Xiang, Y. Zhou, Fatigue behaviour of orthotropic steel bridge stiffened with ultra-high performance concrete layer, J. Constr. Steel Res. 157 (2019) 132–142.
[10] F. Accornero, R. Cafarelli, A. Carpinteri, The cohesive/overlapping crack model for plain and reinforced concrete beams: scale effects on cracking and crushing failures, Mag. Concr. Res. 74 (9) (2022) 433–450.
[11] Z. Zhu, Z. Jiang, F. Accornero, Size-scale and time-scale effects on the failure of UHPC-strengthened reinforced concrete beams, Structures 78 (2025) 109248.
[12] Z. Jiang, Z. Zhu, G. Lacidogna, L.F. Friedrich, I. Iturrioz, Earthquake precursors based on rock acoustic emission and deep learning, Sci 7 (3) (2025) 103.
[13] Z. Zhu, Z. Jiang, F. Accornero, A. Carpinteri, Correlation between seismic activity and acoustic emission on the basis of in-situ monitoring, Nat. Hazards Earth Syst. Sci. 24 (11) (2024) 4133–4143.
[14] C.U. Grosse, M. Ohtsu, Acoustic Emission Testing in Engineering—Basics and Applications, Springer, Heidelberg, Germany, 2008.
[15] M. Ohtsu, Acoustic Emission and Related Non-Destructive Evaluation Techniques in the Fracture Mechanics of Concrete, Woodhead Publishing, Cambridge, UK, 2015.
[16] Z. Jiang, Z. Zhu, F. Accornero, G. Lacidogna, Acoustic emission and digital image correlation evidence of size effects on the compression failure of concrete, Mag. Concr. Res. 77 (17-18) (2025) 1060–1072.
[17] Z. Jiang, Z. Zhu, L.F. Friedrich, E.S. Cezar, J. Chen, G. Lacidogna, I. Iturrioz, Multi-technical analysis of damage process in GFRP-bar reinforced concrete beam, Eng. Struct. 348 (2026) 121803.
[18] A. Carpinteri, G. Lacidogna, M. Corrado, E. Di Battista, Cracking and crackling in concrete-like materials: A dynamic energy balance, Eng. Fract. Mech. 155 (2016) 130–144.
[19] G. Lacidogna, G. Piana, F. Accornero, A. Carpinteri, Multi-technique damage monitoring of concrete beams: Acoustic emission, digital image correlation, dynamic identification, Constr. Build. Mater. 242 (2020) 118114.
[20] D.G. Aggelis, Classification of cracking mode in concrete by acoustic emission parameters, Mech. Res. Commun. 38 (3) (2011) 153–157.
[21] Q. Han, G. Yang, J. Xu, Z. Fu, G. Lacidogna, A. Carpinteri, Acoustic emission data analyses based on crumb rubber concrete beam bending tests, Eng. Fract. Mech. 210 (2019) 189–202.
[22] D. Shi, X. Chen, P. Chen, K. Shang, T. Ji, Revealing the failure mechanism of high strength seawater coral aggregate reinforced concrete slabs based on acoustic emission technology: parameter analysis and DBN-BPNN classification, Eng. Struct. 303 (2024) 117439.
[23] X. Chen, D. Shi, J. Zhang, X. Cheng, Experimental study on loading rate and notch-to-depth ratio effects on flexural performance of self-compacting concrete with acoustic emission and digital image correlation technologies, J. Strain Anal. Eng. Des. 56 (3) (2021) 148–160.
[24] D. Shi, X. Chen, Y. Ning, Damage mechanism analysis of rock-shotcrete under uniaxial compression, Acids Mater. J. 119 (6) (2022) 247–261.
[25] D. Shi, X. Chen, J. Zhang, X. Cheng, W. Li, Z. Shi, C. Wu, Experimental study on post-peak cyclic characteristics of self-compacting concrete combined with AE and DIC techniques, J. Adv. Concr. Technol. 18 (7) (2020) 386–395.
[26] A. Carpinteri, Size effects on strength, toughness, and ductility, J. Eng. Mech. 115 (7) (1989) 1375–1392.
[27] C.G. Hoover, Z.P. Bazant, Universal size-shape effect law based on comprehensive concrete fracture tests, J. Eng. Mech. 140 (3) (2014) 473–479.
[28] Z. Jiang, Z. Zhu, G. Lacidogna, J. Chen, B. Li, Experimental validation and fracture mechanics analysis of an innovative UHPC-based material for structural strengthening, Mech. Res. Commun. 151 (2026) 104603.
[29] Z. Jiang, Z. Zhu, G. Lacidogna, AE monitoring of crack evolution on UHPC deck layer of a long-span cable-stayed bridge, Dev. Built Environ. 23 (2025) 100697.
[30] A. Hillerborg, M. Modéer, P.E. Petersson, Analysis of crack formation and crack growth in concrete by means of fracture mechanics and finite elements, Cem. Concr. Res. 6 (6) (1976) 773–781.
[31] A. Carpinteri, M. Corrado, G. Lacidogna, Heterogeneous materials in compression: correlations between absorbed, released and acoustic emission energies, Eng. Fail. Anal. 33 (2013) 236–250.
[32] A. Carpinteri, F. Accornero, Multiple snap-back instabilities in progressive microcracking coalescence, Eng. Fract. Mech. 187 (2018) 272–281.
[33] JCMS-III B5706, Monitoring method for active cracks in concrete by acoustic emission, Federation of Construction Materials Industries, Japan, 2003.
[34] Recommendation of RILEM TC 212-ACD, Acoustic emission and related NDE techniques for crack detection and damage evaluation in concrete: Test method for classification of active cracks in concrete by acoustic emission, Mater. Struct. 43 (9) (2010) 1187–1189.
[35] M. Ohtsu, T. Isoda, Y. Tomoda, Acoustic emission techniques standardized for concrete structures, J. Acoust. Emiss. 25 (2007) 21–32.
[36] Z. Jiang, Z. Zhu, F. Accornero, Tensile-to-shear crack transition in the compression failure of steel-fibre-reinforced concrete: Insights from acoustic emission monitoring, Buildings 14 (7) (2024) 2039.
[37] B. Gutenberg, C.F. Richter, Frequency of earthquakes in California, Bull. Seismol. Soc. Am. 34 (1944) 185–188.
[38] C.H. Scholz, The frequency-magnitude relation of microfracturing in rock and its relation to earthquakes, Bull. Seismol. Soc. Am. 58 (1968) 399–415.
[39] A. Carpinteri, G. Lacidogna, S. Puzzi, From criticality to final collapse: evolution of the "b-value" from 1.5 to 1.0, Chaos Solitons Fractals 41 (2009) 843–853.
[40] T. Shiotani, K. Fujii, T. Aoki, K. Amou, Evaluation of progressive failure using AE sources and improved b-value on slope model tests, Prog. Acoust. Emiss. 7 (1994) 529–534.
[41] P. Varotsos, N. Sarlis, E. Skordas, Spatio-temporal complexity aspects on the interrelation between seismic electric signals and seismicity, Proc. Athens Acad. 76 (2001) 294–321.
[42] P. Varotsos, N. Sarlis, E. Skordas, Germany. Natural Time Analysis: The New View of Time, Springer, Berlin, 2011.
[43] F. Vallianatos, G. Michas, P. Benson, P. Sammonds, Natural time analysis of critical phenomena: the case of acoustic emissions in triaxially deformed Etna basalt, Phys. A 392 (20) (2013) 5172–5178.
[44] G. Hloupis, I. Stavrakas, E. Pasiou, D. Triantis, S. Kourkoulis, Natural time analysis of acoustic emissions in double edge notched tension (DENT) marble specimens, Procedia Eng. 109 (2015) 248–256.
[45] G. Niccolini, S. Potirakis, G. Lacidogna, O. Borla, Criticality hidden in acoustic emissions and in changing electrical resistance during fracture of rocks and cement-based materials, Materials 13 (2020) 5608.
[46] Q. Han, L. Wang, J. Xu, A. Carpinteri, G. Lacidogna, A robust method to estimate the b-value of the magnitude-frequency distribution of earthquakes, Chaos Solitons Fractals 81 (2015) 103–110.
[47] L.F. Friedrich, E.S. Cezar, A. Colpo, B. Tanzi, G. Lacidogna, I. Iturrioz, Identifying impending failure in heterogeneous materials: a study on acoustic emission time series, Chaos Solitons & Fractals 185 (2024) 115172.
[48] A. Carpinteri, M. Corrado, G. Lacidogna, Three different approaches for damage domain characterization in disordered materials: fractal energy density, b-value statistics, renormalization group theory, Mech. Mater. 53 (2012) 15–28.
[49] G. Lacidogna, F. Accornero, A. Carpinteri, Influence of snap-back instabilities on acoustic emission damage monitoring, Eng. Fract. Mech. 210 (2019) 3–12.
[50] A. Manuello, G. Niccolini, A. Carpinteri, AE monitoring of a concrete arch road tunnel: damage evolution and localization, Eng. Fract. Mech. 210 (2019) 279–287.
[51] S.Y. Alam, A. Loukili, F. Grondin, E. Roziere, Use of the digital image correlation and acoustic emission technique to study the effect of structural size on cracking of reinforced concrete, Eng. Fract. Mech. 143 (2015) 17–31.
[52] B. Pan, Digital image correlation for surface deformation measurement: historical developments, recent advances and future goals, Meas. Sci. Technol. 29 (8) (2018) 082001.
[53] A. Carpinteri, G. Lacidogna, G. Niccolini, S. Puzzi, Morphological fractal dimension versus power-law exponent in the scaling of damaged media, Int. J. Damage Mech. 18 (3) (2009) 259–282.
[54] A. Carpinteri, G. Lacidogna, N. Pugno, Richter's laws at the laboratory scale interpreted by acoustic emission, Mag. Concr. Res. 58 (9) (2006) 619–625.
[55] R. Kotynia, D. Szczech, M. Kaszubska, Bond behaviour of GRFP bars to concrete in beam test, Procedia Eng. 193 (2017) 401–408.
[56] C.E. Shannon, A mathematical theory of communication, Bell Syst. Tech. J. 27 (3) (1948) 379–423.
[57] F. Santo, T. Sattar, G. Edwards, Validation of acoustic emission waveform entropy as a damage identification feature, Appl. Sci. 9 (19) (2019) 4070.
[58] L. Kosteski, I. Iturrioz, G. Lacidogna, A. Carpinteri, Size effect in heterogeneous materials analyzed through a lattice discrete element method approach, Eng. Fract. Mech. 232 (2020) 107041.